Inclination shallowing in Eocene Linzizong sedimentary rocks from Southern Tibet: correction, possible causes and implications for reconstructing the India–Asia collision

Wentao Huang,[1,2] Guillaume Dupont-Nivet,[1,2,3] Peter C. Lippert,[4] Douwe J. J. van Hinsbergen[5] and Erwan Hallot[3]

[1]*Key Laboratory of Orogenic Belts and Crustal Evolution, Ministry of Education, School of Earth and Space Sciences, Peking University, Beijing 100871, China. E-mail: W.Huang@uu.nl*
[2]*Palaeomagnetic Laboratory 'Fort Hoofddijk', Department of Earth Sciences, Utrecht University, Budapestlaan 17, 3584 CD, Utrecht, the Netherlands*
[3]*Géosciences Rennes, UMR 6118, Université de Rennes 1, Campus de Beaulieu, 35042 Rennes Cedex, France*
[4]*Department of Geosciences, University of Arizona, Tucson, AZ 85721, USA*
[5]*Department of Earth Sciences, Utrecht University, Budapestlaan 4, 3584 CD Utrecht, the Netherlands*

SUMMARY

A systematic bias towards low palaeomagnetic inclination recorded in clastic sediments, that is, inclination shallowing, has been recognized and studied for decades. Identification, understanding and correction of this inclination shallowing are critical for palaeogeographic reconstructions, particularly those used in climate models and to date collisional events in convergent orogenic systems, such as those surrounding the Neotethys. Here we report palaeomagnetic inclinations from the sedimentary Eocene upper Linzizong Group of Southern Tibet that are $\sim 20°$ lower than conformable underlying volcanic units. At face value, the palaeomagnetic results from these sedimentary rocks suggest the southern margin of Asia was located $\sim 10°$N, which is inconsistent with recent reviews of the palaeolatitude of Southern Tibet. We apply two different correction methods to estimate the magnitude of inclination shallowing independently from the volcanics. The mean inclination is corrected from $20.5°$ to $40.0°$ within 95 per cent confidence limits between $33.1°$ and $49.5°$ by the elongation/inclination (E/I) correction method; an anisotropy-based inclination correction method steepens the mean inclination to $41.3 \pm 3.3°$ after a curve fitting- determined particle anisotropy of 1.39 is applied. These corrected inclinations are statistically indistinguishable from the well-determined $40.3 \pm 4.5°$ mean inclination of the underlying volcanic rocks that provides an independent check on the validity of these correction methods. Our results show that inclination shallowing in sedimentary rocks can be corrected. Careful inspection of stratigraphic variations of rock magnetic properties and remanence anisotropy suggests shallowing was caused mainly by a combination of syn- and post-depositional processes such as particle imbrication and sedimentary compaction that vary in importance throughout the section. Palaeolatitudes calculated from palaeomagnetic directions from Eocene sedimentary rocks of the upper Linzizong Group that have corrected for inclination shallowing are consistent with palaeolatitude history of the Lhasa terrane, and suggest that the India–Asia collision began at $\sim 20°$N by 45–55 Ma.

Key words: Magnetic fabrics and anisotropy; Palaeomagnetism applied to tectonics; Rock and mineral magnetism; Continental tectonics: compressional; Asia.

1 INTRODUCTION

A shallow bias in palaeomagnetic inclinations recorded in clastic sedimentary rocks has been noted and studied for decades (King 1955; Løvlie & Torsvik 1984; Jackson *et al.* 1991; Tauxe & Kent 2004; Kodama 2009). Palaeolatitudes directly calculated from these inclinations can yield spurious palaeogeographic and tectonic reconstructions. This is especially critical in central Asia, where observed inclinations from redbeds are up to 30° shallower than expected from the reference Apparent Polar Wander Path and lead to very different interpretations of the timing and kinematics of the India–Asia collision (Gilder *et al.* 2001, 2003; Dupont-Nivet *et al.* 2002; Tan *et al.* 2003, 2010; Yan *et al.* 2005; Dupont-Nivet *et al.* 2010a). Although shallow inclinations may be attributed to

non-dipolar geomagnetic field behaviour (Westphal 1993; Chauvin *et al.* 1996; Kent & Smethurst 1998; Si & Van der Voo 2001; Van der Voo & Torsvik 2001; Torsvik & Van der Voo 2002), most of them are clearly attributed to sedimentary processes during deposition and compaction of sediments (Tan & Kodama 1998; Gilder *et al.* 2001, 2003; Bazhenov & Mickolaichuck 2002; Tan *et al.* 2003). Calculating palaeolatitudes from palaeomagnetic inclinations in sedimentary rocks is therefore hindered by the major challenge of recognizing and quantifying inclination shallowing.

A primary boundary condition to estimate the age of the India–Asia collision is the palaeolatitude of the Lhasa terrane, which was the southern edge of the Asian continent since Cretaceous until the collision with India. The growing number of reported palaeolatitude estimates vary widely, from 5°N to 30°N (Westphal & Pozzi 1983; Achache *et al.* 1984; Lin & Watts 1988; Chen *et al.* 1993; Chen *et al.* 2010, 2012; Dupont-Nivet *et al.* 2010b; Liebke *et al.* 2010; Sun *et al.* 2010, 2012; Tan *et al.* 2010; Lippert *et al.* 2011, in press). In the case where estimates are based on palaeomagnetic data from sedimentary rocks, the variability may be partly attributed to palaeomagnetic inclination shallowing. We investigate in this paper the rock magnetic properties of the upper Linzizong Group in the Linzhou basin of the southern Lhasa terrane, which includes continental sedimentary successions that conformably overlie volcanic rocks with well-determined palaeomagnetic directions (Dupont-Nivet *et al.* 2010b). We utilize this rare depositional setting to identify sedimentary inclination shallowing and correct it using two recently developed and independent methods based on: (1) the elongation/inclination (*E/I*; Tauxe & Kent 2004) of the distribution of magnetic directions and (2) the magnetic anisotropy of both susceptibility and remanence (Tan *et al.* 2003; Kodama 2009). The 'corrected' inclinations are compared to the inclinations measured in the coeval and colocated volcanic rocks. We also present the stratigraphy of a broad range of magnetic properties (thermomagnetic runs, hysteresis loops, isothermal remanent magnetization (IRM) component analyses, back-field, FORC diagrams, anisotropy of magnetic susceptibility and anisotropy of anhysteretic remanent magnetization), petrographic descriptions and depositional environments to identify potential sedimentary processes affecting inclination shallowing. Our study provides a basic methodology and understanding of inclination shallowing in Eocene sedimentary rocks from the southern Tibet that also provide additional constraints on the palaeolatitude of the Lhasa terrane.

2 GEOLOGICAL BACKGROUND

The Lhasa terrane is considered to be the southernmost margin of the Eurasian Plate before its Palaeogene collision with the Indian lithosphere (Tapponnier *et al.* 1981; Burg *et al.* 1983; Allegre *et al.* 1984; Burg & Chen 1984; Sengor 1984; Dewey *et al.* 1988; Yin & Harrison 2000). It is separated from the Qiangtang terrane to the north by the Late Jurassic–Early Cretaceous Bangong-Nujiang suture and from the Indian Plate Tethyan Himalaya to the south by the Indus–Yarlung suture (Fig. 1; Dewey *et al.* 1988; Yin & Harrison 2000; Kapp *et al.* 2007). The northward dipping subduction of Neotethyan oceanic lithosphere produced, along the southern margin of the Lhasa terrane, an Andean-type continental margin, characterized by the Gangdese batholith and associated Linzizong volcanic successions (Coulon *et al.* 1986; Yuquans 1995; Ding *et al.* 2003; Mo *et al.* 2008). The Linzizong Group is widely distributed in an east–west elongated area along the northern edge of the Gangdese Belt, and has emplacement ages that range from 69 to 43 Ma (Coulon
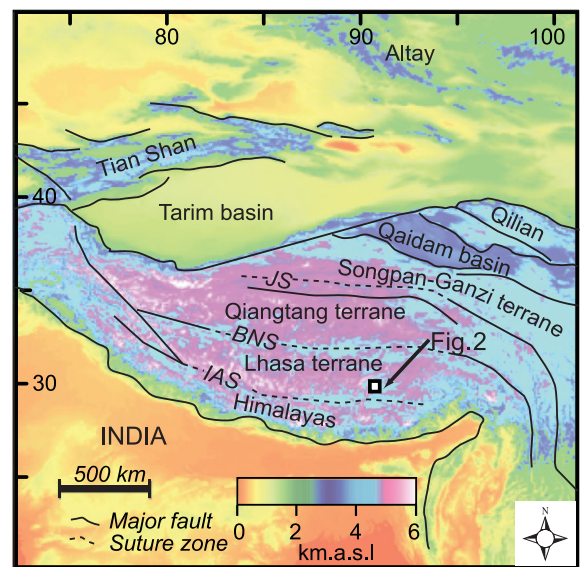

Figure 1. Location of sampling area of Fig. 2 (open white squares) on a shaded relief map of the Tibetan orogen (modified from Dupont-Nivet *et al.* (2008)). IAS, India–Asia suture; BNS, Bangong-Nujiang suture; JS, Jinsha suture.

et al. 1986; Zhou *et al.* 2004; He *et al.* 2007; Lee *et al.* 2009). Thus, the Linzizong Group provides an ideal target for palaeomagnetic investigations of the palaeolatitude history of the Lhasa terrane during the collision.

The Linzizong Group lies unconformably on strongly deformed Mesozoic strata (Leier *et al.* 2007; Mo *et al.* 2007). It is particularly well exposed in the Linzhou basin (Fig. 2; Burg *et al.* 1983; Xu *et al.* 1985; Coulon *et al.* 1986; Mo *et al.* 2003; He *et al.* 2007), where it has a total thickness of ~3500 m and can be divided into the four following distinct units (He *et al.* 2007). The oldest interval, Unit K-T is in unconformable contact with the Cretaceous Takena Formation; it consists of dacitic to rhyolitic ash-tuff layers and andesitic lava flows. Unit K-T is also referred to as the Dianzhong Formation by Chen *et al.* (2010) and Tan *et al.* (2010). Unit T_1 is separated from Unit K-T by a slight angular unconformity. Unit T_1 is composed of two main repeated sequences consisting of conglomerate and sandstone layers at the bottom, then tuffs and thin-layered lime-mudstones and thick ash deposits to the top. Unit T_1 is also referred to as the Nianbo Formation by Chen *et al.* (2010) and Tan *et al.* (2010). Unit T_2, dominated by brown-gray dacitic lapilli tuff, overlies Unit T_1 in a slight angular unconformity. Unit T_3 is characterized by interbedded sandstone, siltstone, mudstone and ash deposits that conformably overlie Unit T_2 (Fig. 3a). Units T_2 and T_3 are also referred to as the Pana Formation by Chen *et al.* (2010) and Tan *et al.* (2010).

Numerous chronostratigraphic studies from the Linzhou basin, based mainly on U-Pb and ^{40}Ar/^{39}Ar radioisotopes methods, have yielded a wide range of emplacement ages for each unit (BGMRXAR 1993; Mo *et al.* 2003; Zhou *et al.* 2004; He *et al.* 2007; Lee *et al.* 2007). U-Pb results yield more precise age constraints compared to ^{40}Ar/^{39}Ar ages, which show larger scatter that may be attributed to the thermal history of the Linzhou basin (He *et al.* 2007). A review of these data indicates that Unit K-T is 69–61 Ma (Zhou *et al.* 2004; He *et al.* 2007), Unit T_1 is 61–54 Ma (Zhou *et al.* 2004), Unit T_2 is 54–44 Ma (BGMRXAR 1993; Zhou *et al.* 2004; He *et al.* 2007). As the youngest reported age from Unit T_2
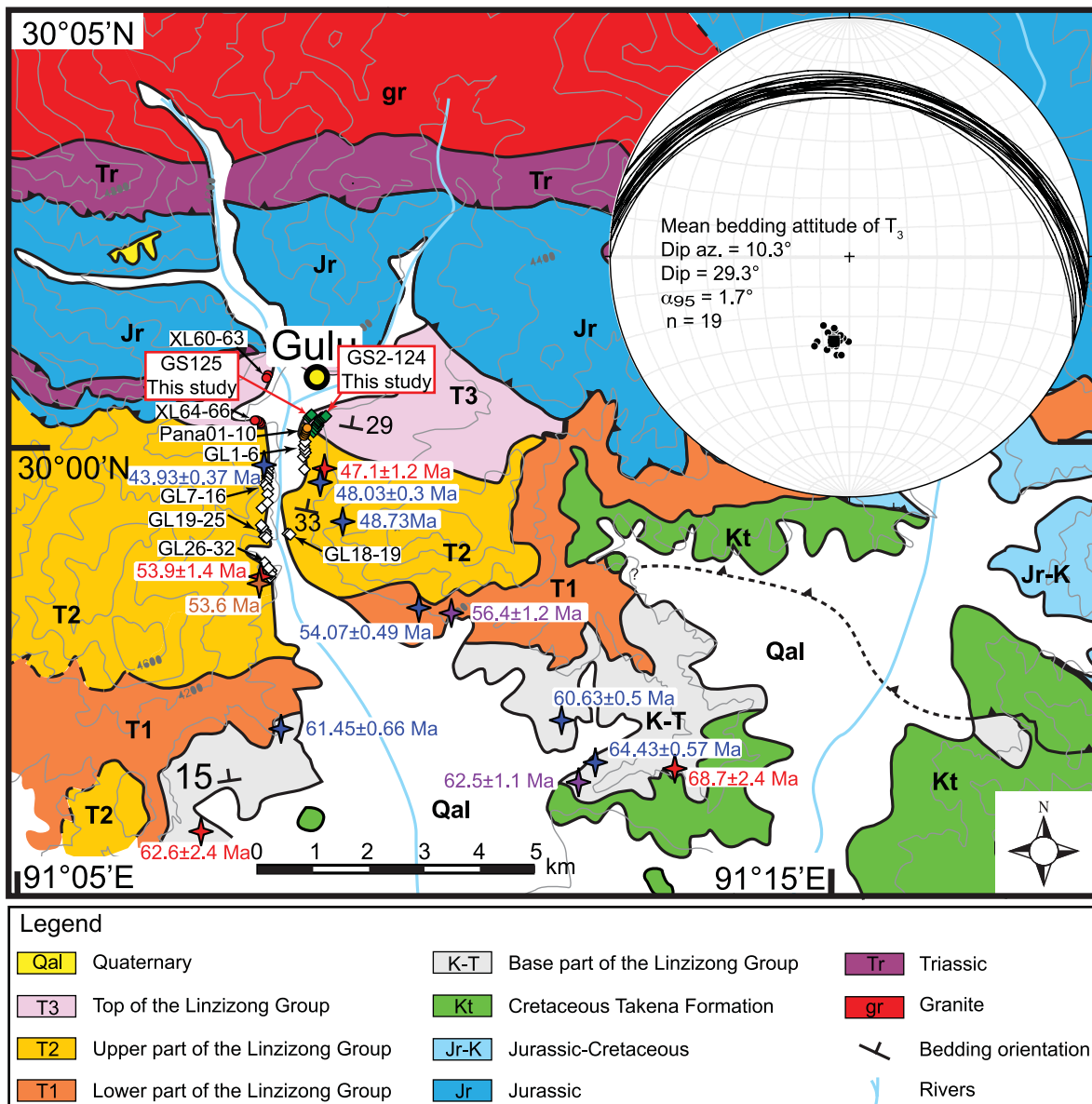
Figure 2. Geochronological and palaeomagnetic sampling locations on simplified geological map on the Linzhou basin (modified from He *et al.* (2007)). Stars represent geochronological sampling locations: red: zircon ages from He *et al.* (2007), purple: zircon ages from Lee *et al.* (2007), blue: Ar–Ar ages from Zhou *et al.* (2004), brown: Ar–Ar ages from BGMRXAR (1993); Diamonds and dots represent palaeomagnetic sampling locations from Unit T_2 and Unit T_3: white diamond: Dupont-Nivet *et al.* (2010b) from Unit T_2, green diamond: this research from Unit T_3; Red dot: Chen *et al.* (2010) from Unit T_3, orange dot: Tan *et al.* (2010) from Unit T_2 in this area.

is 43.93 ± 0.37 Ma (Zhou *et al.* 2004), the deposition of Unit T_3, resting conformably on Unit T_2, probably occurred at *ca*. 43 Ma.

2.1 Description of sampled strata

In this study, we have focused our sampling on Units T_2 and T_3 that provide an ideal archive for comparing palaeomagnetic results from volcanic tuffs and sedimentary rocks. The top of Unit T_2 is composed of silicic welded lapilli-tuff layers, which are interbedded with thin beds of reddish-purple sedimentary rocks. Unit T_2 grades conformably into Unit T_3, which is dominated by reddish-purple sedimentary layers (Fig. 3m). The lower part of Unit T_3 mainly contains pinkish volcaniclastic beds consisting of coarse-grained

sandstone and matrix-supported conglomerates with poorly sorted cobble-sized angular volcanic clasts and some volcanic bombs, suggesting that the volcanic explosions providing pyroclastic fall deposits might have been coeval with the sedimentation. The upper part of the unit consists of medium to fine laminated sandstone, mudstone and dolomitic layers, which often show mud cracks as well as typical fluvial structures such as flute casts, trough cross beds and channels; these sedimentary structures consistently displayed eastward palaeocurrents (Fig. 3). Above the 180 m level of the measured section, the lithostratigraphy is characterized by dolomites and organic-bearing green mudstones, which we interpret as low energy deposits. Sedimentary grain size decreases up-section throughout Unit T_3, to as fine as clay-sized particles (Fig. 3). This trend is also characterized by an up-section decrease in the relative
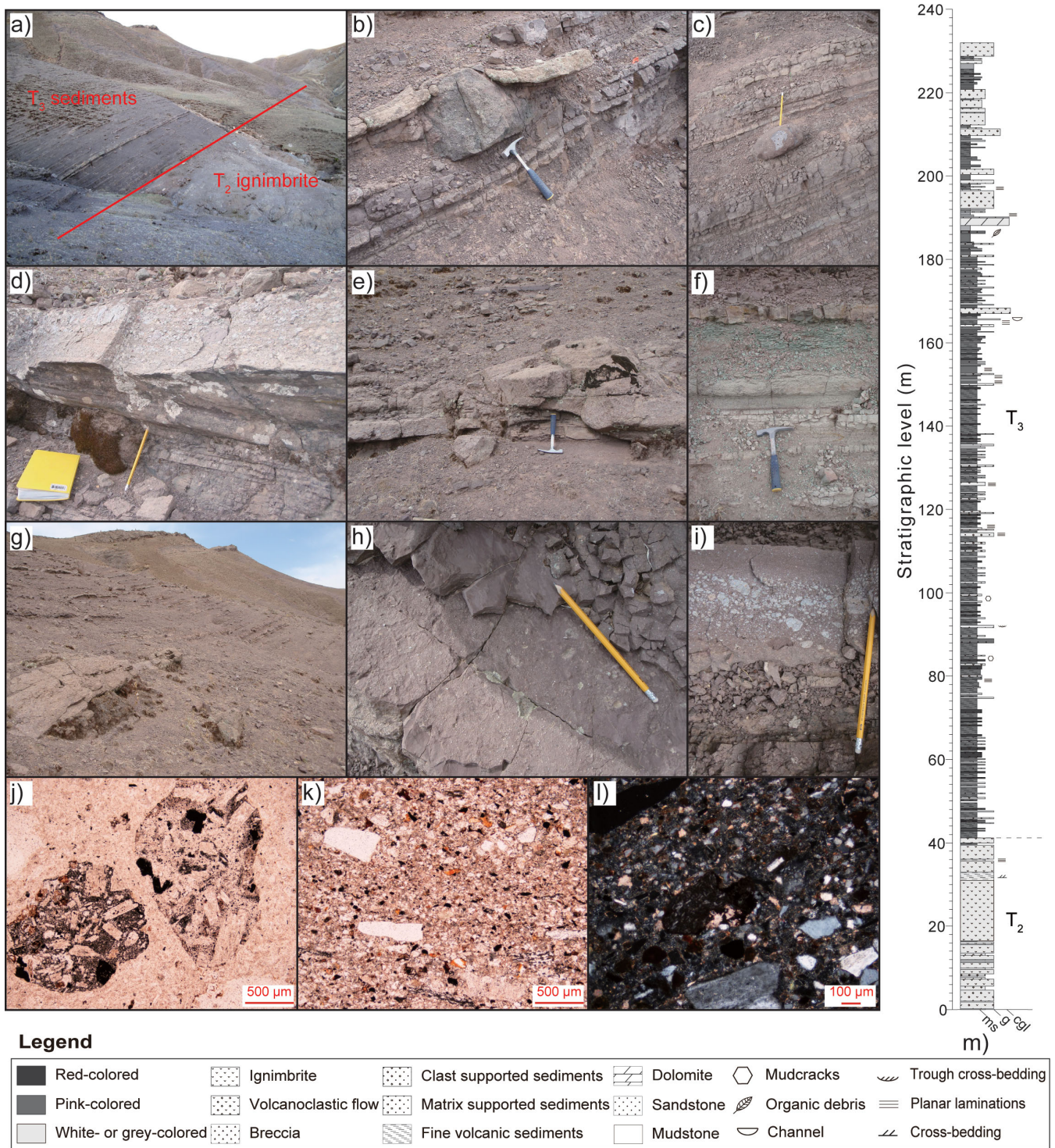
Figure 3. Main field observations, thin section photographs, and stratigraphic section. (a) Conformable contact between Unit T_2 volcanic rocks and Unit T_3 sedimentary rocks. (b and c) Typical fine-grained Unit T_3 sedimentary layers including sparse and large volcanic clasts, interpreted as syn-sedimentary volcanic bombs; stratigraphic levels are 127 and 212.5 m, respectively. (d) Flute casts at stratigraphic level 13.5 m. (e) Trough cross-stratification, indicating palaeocurrents towards the east in Unit T_3; stratigraphic level is 92 m. (f) Green laminated mudstone from the upper part of Unit T_3 at 187 m. (g) Channel formed by east-directed palaeocurrent at 164 m. (h) Mud cracks from Unit T_3 at 84.5 m. (i) Reworked lapilli embayed within a finer-grained laminated volcaniclastic sedimentary layer from Unit T_3 at 157 m. (j) Ignimbrite sample GS13 from top of Unit T_2 (plane polarized light), showing a pyroclastic texture. (k) Sedimentary sample GS63 from Unit T_3 (plane polarized light), showing angular and poorly sorted quartz, feldspar and opaque minerals. (l) Sedimentary sample GS63 from Unit T_3 (crossed polarized light), showing a preferred distribution in the bedding orientation. (m) Lithostratigraphic log of the top of Unit T_2 and Unit T_3. x-axis represents grain size, cgl, conglomerate; g, gravel; ms, medium sandstone.

abundance of volcanic clasts, although discrete tuff layers appear in the topmost part of Unit T_3. We interpret the lithostratigraphic succession to indicate that Unit T_3 was deposited during the waning phases of Eocene volcanism in the southern Lhasa terrane, with the lower part of Unit T_3 deposited in a high-energy fluvial environment and the upper part in a low-energy, possibly lacustrine, environment. During the deposition of Unit T_3, most of the volcanic clasts were thus reworked from earlier eruptions.

2.2 Petrographic description

Detailed petrographic observations from thin sections are consistent with these lithostratigraphic interpretations (Figs 3j, k and l). The tuffs from the top of Unit T_2 have a pyroclastic texture with scattered rock and feldspar lapillis distributed in an ash matrix. The majority of the rock fragments are composed of porphyritic plagioclase and quartz, within a microlithic mesostasis, indicating silicic volcanism. Feldspar is slightly altered to clay minerals and calcite. The opaque minerals (mostly magnetite) are common as an accessory phase in all the samples. The distribution and abundance of the opaque minerals are quite different in the ash matrix and in the volcanic fragments. In the matrix, opaque phases are scarce and randomly distributed, whereas in the fragments, opaque minerals are numerous and usually appear along the edges of feldspar crystals.

The sedimentary rocks of Unit T_3 are mostly arkosic litharenite. Plagioclase and quartz are the main detrital minerals. Other minor detrital minerals include biotite, epidote and sphene. Clasts are usually angular in shape and poorly sorted indicating limited transport from the source. When elongated they show a preferred orientation parallel to bedding. Carbonate minerals occur as either pore-filling cement or partial replacement of feldspar. Clay minerals and iron hydroxides are observed in some thin sections. Recrystallization is limited, affecting only the very edge of some fine quartz grains. The boundaries of detrital grains are sharply defined, indicating limited transport from the source. Recrystallization is limited to the very edge of some fine quartz grains. Based on the thin section observations, both the tuff from Unit T_2 and sedimentary rocks from Unit T_3 show little sign of alteration, but sediments of Unit T_3 appear to be slightly more altered than the tuff of Unit T_2.

3 PALAEOMAGNETIC SAMPLING

In order to thoroughly investigate and compare palaeomagnetic properties of volcanic rocks and sedimentary rocks our study focuses here on comparing results from the volcanic T_2 unit to results from the overlying T_3 sedimentary unit. For Unit T_2, 37 ignimbrite sites (241 oriented cores, GL1–GL32, GS2, GS4, GS9, GS11 and GS22) were presented in Dupont-Nivet et al. (2010b). These data are complemented by seventeen single cores in ignimbrites (GS1, GS3, GS5, GS6, GS7, GS8, GS10, GS12–GS21) sampled in stratigraphic succession at the top of Unit T_2 just below the sediments of Unit T_3. We also present results from 139 oriented sediment cores collected in stratigraphic succession across Unit T_3 (GS23–GS121 and GS125.1–GS125.31), as well as from three tuff sites (23 oriented cores, GS122-GS124) from the top of this unit (Fig. 2). Typical 2.5 cm diameter palaeomagnetic cores were collected using a portable gasoline-powered drill and oriented with magnetic and sun compasses. Bedding attitudes determined from the planar orientation of the top surface of the sedimentary layers were measured with a Brunton compass at several sampling sites. The observed variations in the orientations of measured sedimentary bedding are very small

within the unit; therefore, we calculate and apply the mean bedding correction (dip azimuth = 10.3°N, dip = 29.3°; α_{95} = 1.7°) from 19 measurements to all samples from Unit T_3 (Fig. 2; Table S1). The resulting bedding attitude of Unit T_3 is statistically indistinguishable from the one measured throughout the T_2 volcanic unit below (Dupont-Nivet et al. 2010b).

4 ROCK MAGNETISM

We complete several rock magnetic experiments to characterize the magnetic properties and identify the carrier(s) of the magnetization of the various sampled rocks. Each of these experiments is described later.

4.1 Thermomagnetic runs

Both high-field and low-field thermomagnetic experiments have been completed on selected samples from top of Unit T_2 volcanic rocks and Unit T_3 sedimentary rocks. High-field thermomagnetic runs (magnetization versus temperature) were measured in air by a house-built horizontal translation type Curie balance with a sensitivity of approximately 5×10^{-9} Am^2 (Mullender et al. 1993). Approximately 40–70 mg of six powdered samples from representative lithologies were put into a quartz glass sample holder and were held in place by quartz wool; heating and cooling rates were 10 °C min^{-1}. Stepwise thermomagnetic runs were carried out with intermittent cooling between successive heating steps. The successive temperatures were 150, 250, 400, 500 and 700 °C, respectively. Low-field thermomagnetic experiments (susceptibility versus temperature) were also performed on dry bulk material from the same samples using the KLY3-CS susceptibility bridge. Several stepwise thermomagnetic runs were also performed as the Curie balance measurement, but with successive temperature steps of 350, 450 and 700 °C.

Samples from Unit T_2 volcanic rocks are characterized by two components distinguished in both magnetization and susceptibility runs (Figs 4a and b): a low-temperature component (LTC = ∼250–400 °C) and a high-temperature component (HTC = 525–600 °C). More than 80 per cent of the magnetization and susceptibility have been lost after multiple heating and cooling cycles. Following Dupont-Nivet et al. (2010b) and based on previous rock magnetic experiments on similar rocks of Unit T_2, we interpret the LTC to be associated to Ti-rich titanomagnetite and/or oxidation of primary magnetite. In contrast, the HTC is interpreted as mainly magnetite. The presence of meta-stable Ti-rich titanomagnetite may indicate fresh and unaltered particles (Appel & Soffel 1984).

Thermomagnetic runs yield substantially different results for Unit T_3 sedimentary rocks (Figs 4c–h). Magnetization gradually decreases from ∼275 to 550 °C with rapid decrease observed from 400 to 550 °C in high-field thermomagnetic runs. Low-field magnetic susceptibility for all the samples generally increases from room temperature up to 450 °C and then decreases rapidly between 450 and 580 °C. Some samples show additional loss of susceptibility up to 700 °C. For sample GS79 and GS125.5 the magnetic susceptibility remains relatively high at T = 700 °C, which may result from the contribution of paramagnetic material like clay minerals (Figs 4f and h). All the samples show irreversible heating and cooling curves and decrease in both susceptibility and magnetization with increasing temperature up to ∼700 °C. We interpret these magnetic behaviours to indicate the presence of Ti-poor titanomagnetite with various degree of titanomagnetite oxidation (maghaemite) and minor presence of haematite (Dunlop & Ödemir 1997).
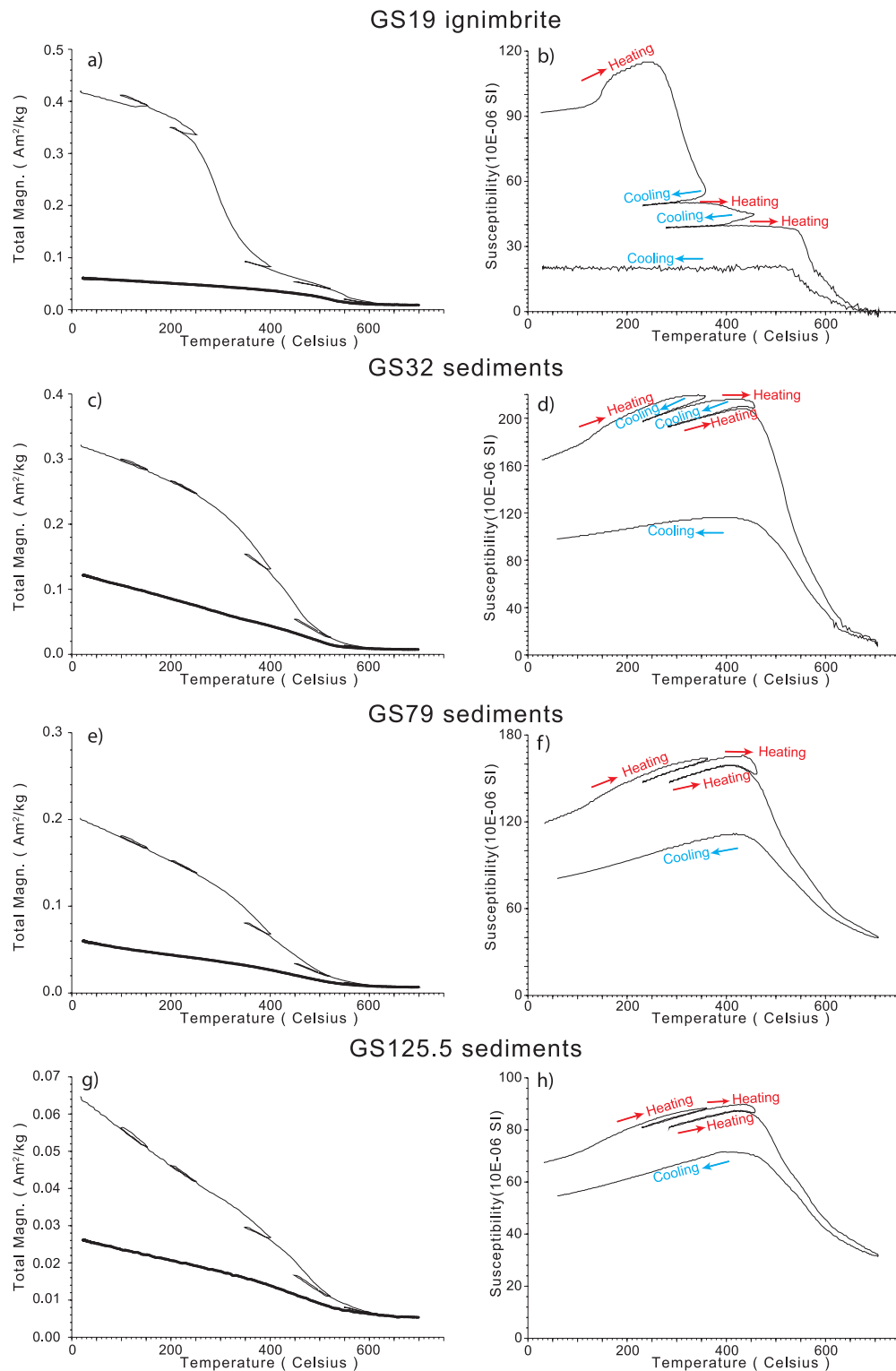
Figure 4. High-field thermomagnetic runs (a, c, e and g) on Curie balance (Mullender *et al.* 1993) and low-field thermomagnetic runs susceptibility versus temperature (b, d, f and h) on Kappabridge KLY3-CS for typical samples from Unit T_2 (GS19) and Unit T_3 (GS32, GS79 and GS125.5) samples. In the high field thermomagnetic curves, thick (thin) lines indicate the heating (cooling) curves; in the low field thermomagnetic curves, arrows indicate heating (red) and cooling (blue). All measurements were performed in air.

4.2 Hysteresis loops, IRM and back-field and first order reversal curve diagrams

An alternating gradient magnetometer (MicroMag Model 2900— Princeton Measurements Inc, noise level 2×10^{-9} Am^2) operating

at room temperature was used to measure (in the following order): (1) hysteresis loops, (2) IRM acquisition curves, (3) back-field curves and (4) first order reversal curves (FORC) diagrams, for 10 representative samples. Sample chip masses ranged from 50 to

70 mg. We used a maximum applied field of 2 T, a field increment of 10 mT, and an averaging time of 0.15 s. Hysteresis loops were measured to determine the saturation magnetization (M_s), the saturation remanent magnetization (M_r), coercive force (B_c) and remanent coercivity (B_{cr}). These parameters were determined after correcting for the paramagnetic contribution of the sample and probe. To further assess the magnetic domain state, the presence of magnetic interactions and the magnetic mineralogy, FORCs were also measured. For each FORC diagram, 200 curves were measured with an averaging time of 0.15 s per data point. The FORC diagrams were processed by an in-house developed program (FORC_Analysis.exe, by Tom Mullender) at the 'Fort Hoofddijk' Palaeomagnetic Laboratory.

For Unit T_2 volcanic rocks, the hysteresis loop is closed below 500 mT but it is not yet saturated (Fig. 5a). The IRM curves show saturation below 600 mT (Fig. 5b). These observations, as well as the low B_c and B_{cr} values, indicate the dominance of a low-coercivity component. The FORC diagram for sample GS19 shows a divergent pattern of the outer five contours that is characteristic of multidomain (MD) grains. However, the inner contours are somewhat less divergent and the FORC diagram is less symmetrical than those for typical MD samples (Fig. 5c). Therefore, the state of the magnetic carrier can be interpreted to be close to pseudo-single domain (PSD; Pike *et al.* 1999; Roberts *et al.* 2000). This interpretation is consistent with magnetic carrier state defined by B_{cr}/B_c and M_r/M_s (Dunlop 2002).

For Unit T_3 sedimentary rocks, the hysteresis loops are narrow-waisted (Figs 5d, g and j). B_c and B_{cr} values range from 7.26 to 13.28 mT and 25.8 to 35.59 mT, respectively (Table S2). The lower B_c and B_{cr} are consistent with Ti-poor titanomagnetite as the main ferromagnetic mineral. However, an incomplete saturation of hysteresis loops and IRMs above 600 mT (Figs 5j and k) indicates a minor contribution of a high-coercivity mineral, such as haematite or goethite. B_{cr}/B_c and M_r/M_s indicate a PSD mean magnetic grain size (Dunlop 2002). FORC diagrams for Unit T_3 sedimentary rocks have divergent and symmetrical contours with very low coercivities (Figs 5f, i and l), consistent with a population of interacting PSD state of the main magnetic minerals (Pike *et al.* 1999; Roberts *et al.* 2000).

4.3 IRM component analysis

We supplement our hysteresis loop measurements and quantitatively assess contributions of different magnetic minerals to magnetization with IRM component analysis. Both Unit T_2 volcanic rocks and Unit T_3 sedimentary rocks were analysed using different components to fit the IRM acquisition curves following the cumulative log-Gaussian approach (Kruiver *et al.* 2001).

The IRM acquisition curves for Unit T_2 ignimbrite are fit with three IRM components: component L_1 with $B_{1/2}$ (the field at which half of SIRM is reached) of 4 mT, soft component L_2, and a harder component L_3, with $B_{1/2}$ of 28.2 and 95.5 mT, respectively (Fig. 6a). Component L_1, a very low-coercivity component, constitutes only $\sim$2 per cent of the SIRM; it is only required to fit the skewed-to-the-left distribution of component L_2 and is not given physical meaning other than being the result of thermally activated component L_2 particles. Component L_2 and component L_3 typically represent Ti-poor titanomagnetite and Ti-rich titanomagnetite, respectively. The contribution of Ti-poor titanomagnetite to the saturation isothermal remanent magnetization (SIRM) is approximately 31.5 per cent, whereas the contribution of Ti-rich titanomagnetite is approximately 66.7 per cent (Table S3).

For the T_3 sedimentary rocks, the IRM acquisition curves are also best fit with a very low-coercivity component S_1 ($B_{1/2}$ lower than 9 mT) and a soft component S_2 with low $B_{1/2}$ between $\sim$25 and $\sim$40 mT. We found that a high-coercivity component S_3 with a much higher $B_{1/2}$ changing from $\sim$400 to $\sim$650 mT and a stable dispersion parameter (DP) approximately 0.4 (log units) is required to fit the curves (Figs 6b–d; Table S3). Similar to results from Unit T_2 volcanic rocks, component S_1 also does not have a physical meaning. Component S_2 with a low $B_{1/2}$ is consistent with Ti-poor titanomagnetite. The small dispersion for this component (DP: 0.30–0.36, log units) indicates a narrow grain size distribution. IRM component analyses also indicate that this component is the dominant magnetic carrier, with the contribution to SIRM approaching 90 per cent (except GS24; see Table S3). We interpret component S_3 to be haematite because the $B_{1/2}$ value for haematite typically ranges from 300 to 800 mT (Kruiver & Passier 2001); it contributes approximately 8 per cent to the total SIRM (except GS24 and green mudstone GS102B, component S_3 of which contributes 18.1 and 3.5 per cent to the SIRM, respectively; Table S3). Apart from the magnetic susceptibility decay from 600 to 700 °C, we note that haematite is poorly resolved in the high-field thermomagnetic runs and FORC diagrams because magnetite, with much stronger magnetization than haematite, obscures the signal of haematite, even when the haematite fraction is up to 18.1 per cent as in sample GS24.

These interpretations from IRM component analysis are consistent with results from other rock magnetic experiments. The magnetization of T_2 volcanic rocks is carried by Ti-poor and Ti-rich titanomagnetite. The predominant magnetic carrier in T_3 sedimentary rocks, however, is larger-grained Ti-poor titanomagnetite, with contributions of oxidized products such as maghaemite and a minor input from haematite.

5 DEMAGNETIZATIONS AND CHRM DIRECTION ANALYSES

5.1 Demagnetizations

We have isolated characteristic remanent magnetization (ChRM) directions using both thermal and AF demagnetization. Samples were heated and cooled in a magnetically shielded, laboratory-built furnace that has a residual field less than 10 nT. The natural remanent magnetization (NRM) was measured on a 2G horizontal Enterprises DC SQUID cryogenic magnetometer (noise level 3×10^{-12} Am^2). Initial susceptibility before demagnetization was also measured. AF demagnetizations were applied with an in-house developed robotized sample handler (Mullender *et al.* 2005) attached to a horizontal pass-through 2G Enterprises DC SQUID magnetometer (noise level 1×10^{-12} Am^2) hosted in the magnetically shielded room (residual field <200 nT) at Fort Hoofddijk Palaeomagnetic Laboratory, Utrecht University. Samples were progressively demagnetized by stepwise thermal or AF treatment (thermal steps: 150, 200, 250, 300, 350, 425, 450, 475, 500, 525, 550, 575, 600, 625, 650, 660, 670, 675, 680, 685 and 690 °C; AF steps: 5, 10, 15, 20, 25, 30, 40, 45, 50, 55, 60, 65, 70, 80 and 90 mT).

For the Unit T_2, palaeomagnetic results from volcanic samples were previously described in Dupont-Nivet *et al.* (2010b). Here we analyse seventeen additional volcanic samples that are close to the transition with Unit T_3 (Fig. 7a). These demagnetization behaviours are the same as described by Dupont-Nivet *et al.* (2010b) for the other T_2 volcanic rocks. A component is unblocked between
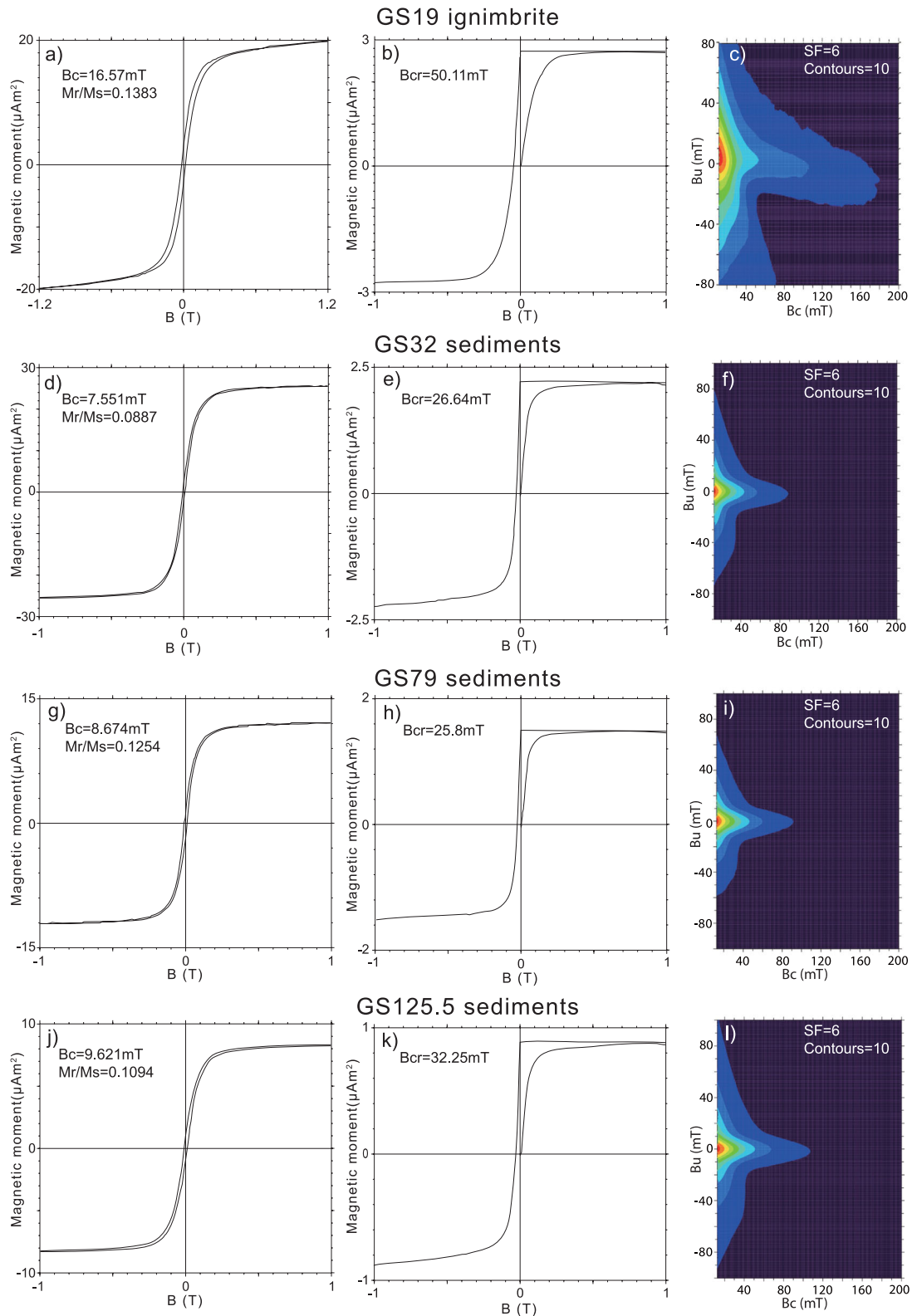
Figure 5. Hysteresis loops (a, d, g and j), IRM and back-field curves (b, e, h and k) and FORC diagrams (c, f, i and l) for characteristic samples from Unit T_2 (GS19) and Unit T_3 (GS32, GS79 and GS125.5) samples. The hysteresis loops, IRM curves, and backfield curves were measured for $-2T = B = 2T$. Hysteresis loops are corrected for the paramagnetic contribution. The sample codes are indicated at the top of each diagram and magnetic parameters can be found in the top-left part (M_s: saturation magnetization, M_r: remanent saturation magnetization and B_c: coercive force). The FORC diagrams indicate the smoothing factors (SF) used to process the data; each diagram is presented with 10 contours levels.
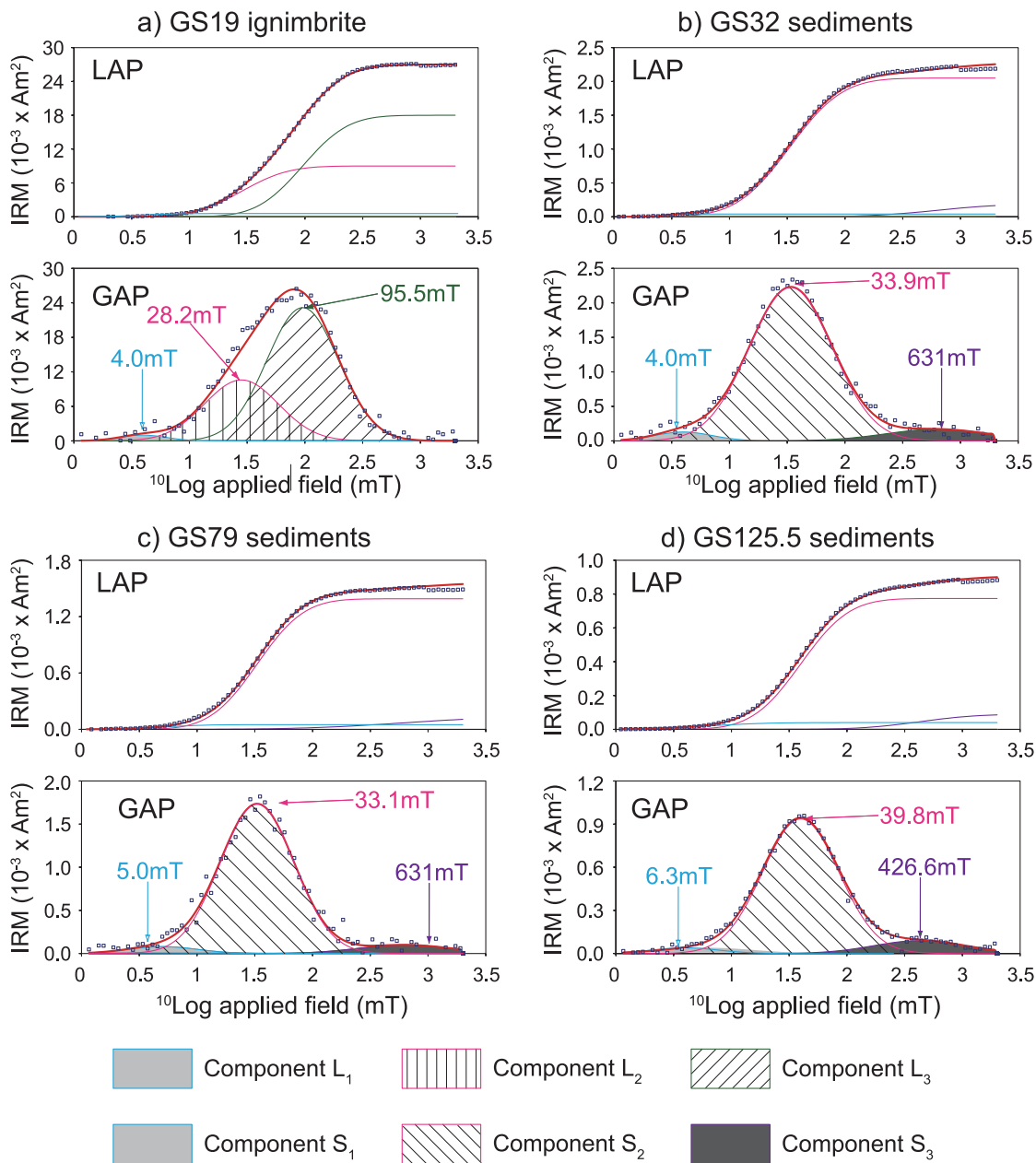
Figure 6. Representative examples of the IRM component analysis (Kruiver *et al.* 2001). Squares are measured data points. The components are marked with different lines: the linear acquisition plot (LAP) and the gradient acquisition plot (GAP) are shown in hatches. Component 1 has a very low coercivity, component 2 and 3 are relatively soft, component 4 has the highest coercivity. SIRM is in Am^2, $\log_{10} (B_{1/2})$ and DP are in $\log_{10}$ mT. Values of $B_{1/2}$ are displayed in each panel. GS19 is the ignimbrite from Unit T_2; GS32, GS79 and GS125.5 are all sedimentary rock from Unit T_3.

550 and 575°C and 30–60 mT, and a component with a lower unblocking temperature (<350 °C) but a higher coercivity (>60 mT) is also isolated. These two components give the same ChRM directions.

For the sedimentary rocks of Unit T_3, one component is commonly removed at low temperature (150–200 °C) or low field level (10 mT) by thermal and AF treatment (Fig. 7c), respectively. The random direction of this component suggests it is a laboratory-induced viscous remanent magnetization. After removing this viscous overprint, most samples revealed a clear ChRM that is unblocked between 275 and 550 °C and 10–50 mT for thermal and AF treatment, respectively (Figs 7c–f). These unblocking demagne-

tization levels are consistent with our rock magnetic interpretations that indicate the ChRM is mainly carried by Ti-poor titanomagnetite with minor contribution from maghaemite. The three volcanic sites (GS122–GS124) from the top of Unit T_3 show anomalous NRM directions and extremely high NRM intensities (up to 200 A m^{-1}); these samples are probably affected by lightning given their rapid decay of NRM at low field (<10 mT) and high altitude in the section. We exclude these results from further analyses. In general, AF demagnetization yielded well-defined linear demagnetization paths, whereas thermal demagnetization often resulted in erratic demagnetization trajectories presumably associated with oxidation during heating (Figs 7d and f).
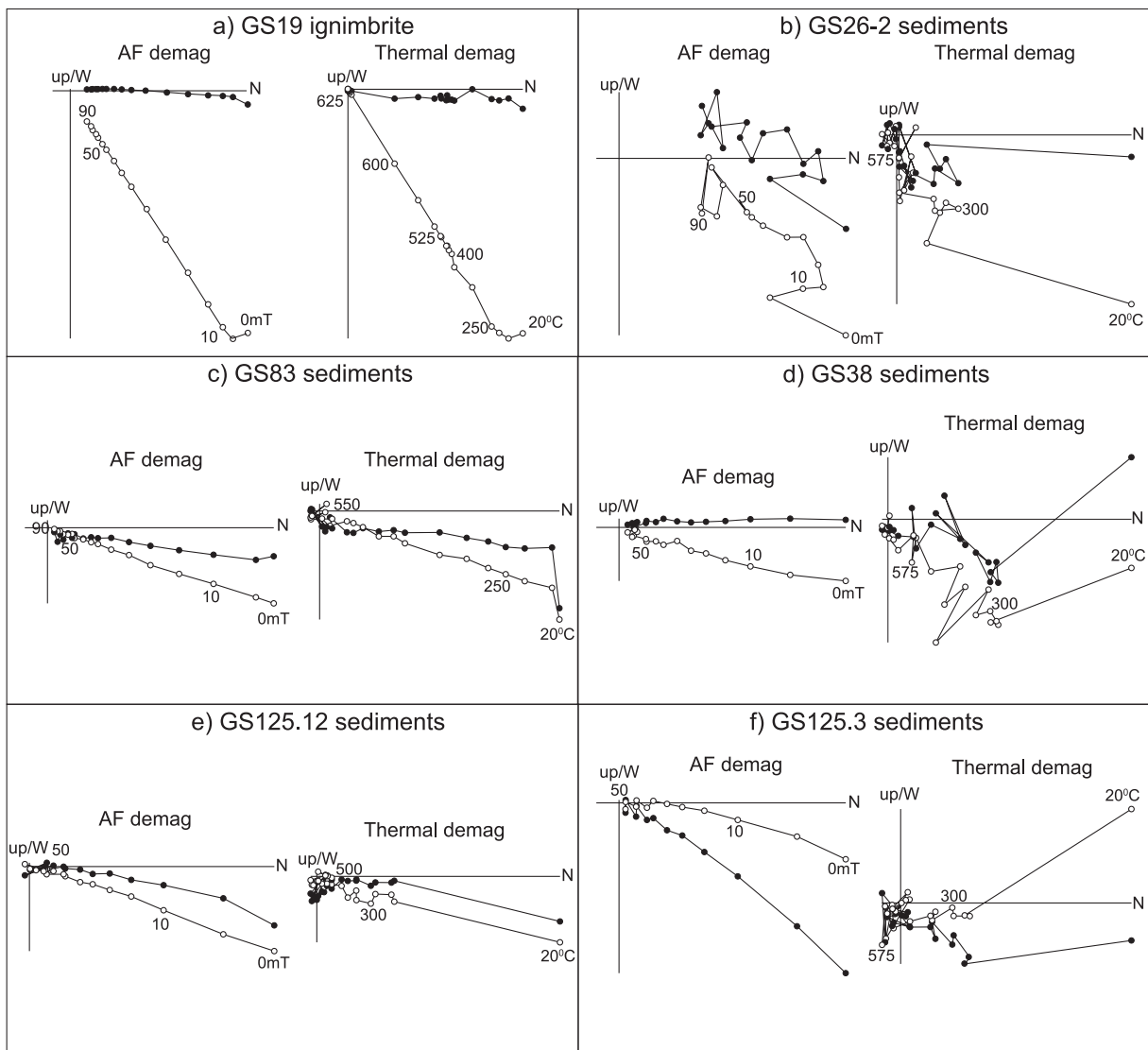
Figure 7. Comparison of alternating field (af) and thermal demagnetization diagrams for the typical Unit T_2 (GS19) and Unit T_3 (GS26–2, GS83, GS38, GS125.12 and GS125.3) samples. Closed (open) symbols represent the projection of vector end-points on the horizontal (vertical) plane; values represent alternating field and thermal demagnetization steps in mT (millitesla) and °C, respectively. All diagrams are displayed after bedding tilt correction. Both af and thermal demagnetization provide interpretable ChRM directions (a, c, and e), but usually af demagnetization yields more linear paths than thermal demagnetization (d and f); sometimes neither af nor thermal demagnetization yield interpretable ChRM directions (b).

5.2 ChRM directions

Some samples displayed erratic demagnetization paths that yield no interpretable directions, but the majority of samples display a high-temperature/high-coercivity direction that decays linearly towards the origin (Fig. 7). Principal component analysis (Kirschvink 1980) on at least five successive steps resulted in precisely determined ChRM directions for most of these samples (Table S4). Thermal and AF demagnetization paths for specimens from the same sample were usually comparable (Figs 7c and e), although thermal demagnetization results were sometimes more erratic and yielded higher maximum angular deviation (MAD) values or no interpretable directions (Figs 7b, d and f). Directions with MAD > 10° were systematically rejected from further analysis. Virtual geomagnetic poles (VGPs, assuming a 100 per cent dipolar geomagnetic field) calculated from these remaining directions that were more than 45° from the mean VGP direction were iteratively rejected until there were no

outliers. For samples with ChRM directions determined from AF and thermal demagnetization protocols, we chose the AF results for further analysis because these results yielded more precise directions than thermal demagnetizations. Our final palaeomagnetic data set consists of 100 AF ChRM directions and 19 thermal ChRM directions; the latter are from samples with only thermal demagnetization results. Fisher (1953) statistics were used to evaluate the VGPs computed form the interpreted palaeomagnetic directions; our analysis follows Deenen *et al.* (2011).

The overall mean ChRM direction of the final 119 samples is $D_g = 10.2°$, $I_g = 49.8°$ ($k_g = 25.1$, $\alpha_{95} = 2.6°$) in geographic coordinates and $D_s = 10.2°$, $I_s = 20.5°$ ($k_s = 25.1$, $\alpha_{95} = 2.6°$, with a corresponding palaeolatitude $\lambda = 10.6°N$) after tilt correction (Figs 8a and b; Table S4). The A_{95} value of the mean VGP of all 119 directions is 2.5°, which falls just within the range of A_{95} values ($A95_{min/max}$ of 2.5°/4.0°) defined as a reliability envelope by Deenen *et al.* (2011). This implies that the observed scatter can be explained
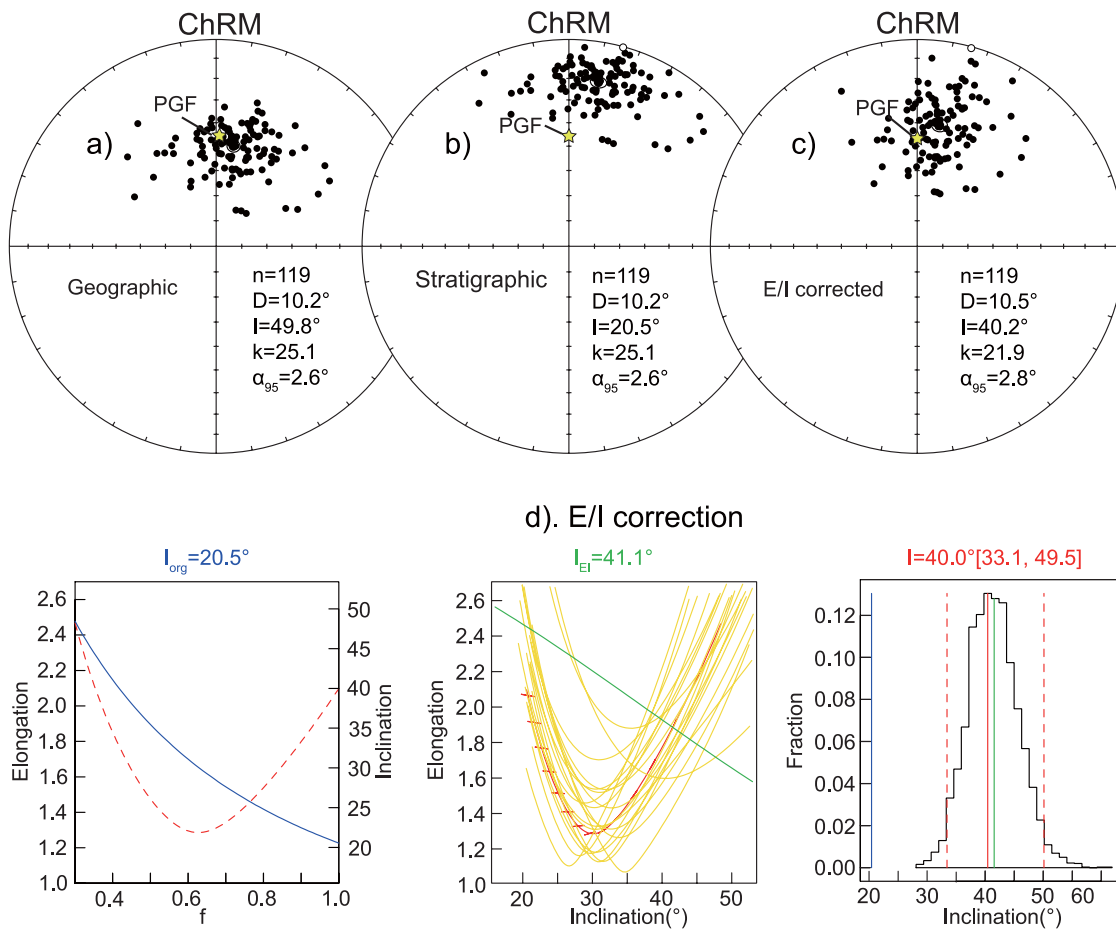
Figure 8. Equal-area projections of individual characteristic remanent magnetization (ChRM) directions before (a) and after (b) bedding tilt correction for T_3 sedimentary rocks, see Table S4 for the data selection. (c) Equal-area projections of the individual ChRM directions after E/I correction. (d) Correction for the inclination error using the E/I method developed by Tauxe & Kent (2004). Plot of elongation versus inclination for the TK03.GAD model shown on left, where the red barbed curve shows the variation of the elongation of the data set distribution with respect to mean inclination when affected by flattening factor ranging from 0.3 to 1; green curve is the same for data set generated from 1000 bootstrap analyses. The corrected inclination is given by the intersection with the green line (expected elongation from the TK03.GAD). Right-hand fraction/inclination plot indicate the distribution of the corrected inclinations with 95 per cent confidence limit. PGF—present geomagnetic field.

by secular variation, which indicates that the sediments have adequately recorded the geomagnetic field at the time of deposition.

We cannot assess the primary origin of the ChRM using standard field tests because bedding attitudes are uniform throughout the sampled section and because all the ChRM directions are of exclusively normal polarity. Before bedding tilt correction, the ChRM directions show a cluster which differs clearly from the geocentric axial dipole field direction for the present latitude of the section with the difference in declination of $10.2 \pm 2.5°$, although the CTMD (common true mean direction) test is indeterminate since it involves a single observation test (Fig. 8a). After bedding correction the observed ChRM directions display low inclinations (compared to the underlying volcanic rocks) with a clear east–west elongated distribution typical of inclination flattening usually observed from primary remanent magnetization in sedimentary rocks. These rather suggest acquisition of the magnetization during or soon after deposition of the sediments. This assertion is further indicated by the analyses described later.

Assuming that the ~43 Ma age estimate of Unit T_3 is correct, the normal polarity uniformly found throughout Unit T_3 implies that it has been deposited in Chron C20n of the geomagnetic polarity timescale (GPTS), which is dated at 43.505–42.351 Ma (Gradstein

et al. 2012). This would also imply that the whole Unit T_3, which is about 200 m thick, has been deposited in less than 1 Myr with accumulation rates of at least 17 cm kyr^{-1} that are in line with the observed lithologies and depositional environment.

5.3 Elongation/inclination (*E/I*) correction

The E/I correction based on the statistical palaeosecular variation models of the geocentric axial dipole magnetic field (Tauxe & Kent 2004) was applied to the T_3 sedimentary data set. The mean inclination is corrected from $20.5 \pm 2.6°$ to $40.0°$ with 95 per cent confidence limits between $33.1°$ and $49.5°$ (Figs 8c and d). This direction is statistically indistinguishable from the tilt-corrected direction measured in the underlying T_2 volcanic unit ($40.3 \pm 4.5°$; Dupont-Nivet *et al.* 2010b). The identical inclinations of Unit T_2 volcanic rocks and of the E/I-corrected sedimentary directions suggest that indeed inclination shallowing has affected the ChRM of Unit T_3 sedimentary rocks. The E/I correction indicates that the ChRM directions do have a primary origin acquired during or shortly after deposition and was subsequently flattened. Moreover, the corrected VGP distribution has an A_{95} of 2.7°, falling well within the confidence envelope (Deenen *et al.* 2011), provides further

support to a reliable and primary recording of secular variation by the sediments. These interpretations are corroborated by analyses of magnetic anisotropy, which are described next.

6 MAGNETIC ANISOTROPY

6.1 AMS and AARM

We measured the magnetic anisotropy of the sampled rocks to explore possible causes for the inclination shallowing. First, we determined the composite fabric of the paramagnetic, diamagnetic and ferromagnetic grains by measuring the anisotropy of magnetic susceptibility (AMS) of 125 sedimentary samples from Unit T_3 and 176 volcanic samples from Unit T_2 using an AGICO KLY-3S AC susceptibility meter (Table S5). The anisotropy of anhysteretic remanent magnetization (AARM) of 110 sedimentary samples from Unit T_3 and 9 volcanic samples from the top of Unit T_2 were also measured to quantify the fabric of the ferromagnetic grains (Table S6). An anhysteretic remanent magnetization (ARM) was applied to each sample in the 5–60 mT coercivity window with a 0.05 mT DC field using a 2G Enterprises demagnetizer. The coercivity spectra of ferromagnetic grains were determined from partial anhysteretic remanence magnetization (pARM) and from AF demagnetization. The procedure consists of cycles of ARM acquisition, measurement and demagnetization along six positions (X, $–X$, Y, $–Y$, Z, $–Z$) for each sample, as described by McCabe *et al.* (1985). A 60 mT AF field was applied together with the 0.05 mT DC field parallel to the axis of the AF field; both AF and DC fields decreasing smoothly in intensity such that the resulting remanence is parallel to the DC field. The ARM intensity is the average remanence in the six measured directions. Both AMS and AARM measurements involve the calculation of a triaxial ellipsoid with principal axes K_{max}, K_{int} and K_{min}. We express the magnetic fabric using the following parameters: the degree of anisotropy, P (K_{max}/K_{min}); the lineation, L (K_{max}/K_{int}); the foliation, F (K_{int}/K_{min}); and the shape parameter, T ($T = (\ln F - \ln L)/(\ln F + \ln L)$), which varies from prolate (–1) to oblate (+1), as proposed by Jelinek (1981).

The AMS measurement of Unit T_3 sedimentary rocks shows that the anisotropy degree (P) ranges from 1.018 to 1.13 with a mean value of 1.046. This value is much higher than P values of Unit T_2 volcanic rocks (∼1.027; Fig. 9; Table S5). AARM analysis yields similar results, with even higher P values that range from 1.038 to 1.224 with a mean value of 1.095 (Fig. 9; Table S6). These results indicate that the AMS is dominated by the minerals carrying the remanent magnetization (i.e. ferromagnetics), which is expected for magnetite type carriers such as found in the T_3 sedimentary rocks because the susceptibility of magnetite is several orders of magnitude greater than other minerals typically found in rocks (Collinson 1983). This is also indicated by the high k values of the studied specimens (Tarling & Hrouda 1993). The lineation (L) is weak compared to the foliation (F) observed in both AMS and AARM (Fig. 9).

The magnetic anisotropy fabric for the entire T_3 sedimentary section is characterized by oblate ellipsoids (Fig. 9). Minimum axes cluster nearly perpendicular to bedding and maximum and intermediate axes are dispersed around the horizontal (Fig. 10). This typical sedimentary fabric (Hrouda 1991) is not observed in AMS results from Unit T_2 volcanic rocks, indicating that there is no discernable fabric in the igneous unit at this stratigraphic height. The mean values of K_{min} inclinations from the AMS and AARM measurements of the T_3 sedimentary rocks are deflected approximately 10° east-

wards from the pole of the bedding plane (Figs 10d and f). This orientation is nearly perpendicular to what would be expected from strain associated with the regional north-south directed shortening; therefore, we conclude that the anisotropy fabric is not a function of tectonic strain origin. However, these magnetic fabrics are clearly recognized in both experimental and theoretical depositional studies to be related to compactional loading and palaeocurrents, with the latter tilting the magnetic minerals due to imbrication (Rees 1961, 1965; Rees & Woodall 1975; Hrouda 1991; Housen *et al.* 1993; Pares *et al.* 1999; Gilder *et al.* 2001). This easterly tilted K_{min} direction observed in the T_3 sedimentary rocks is consistent with our observations of west to east palaeocurrent flow directions determined from flute casts and channel orientations throughout the sedimentary section (Figs 3d, e and g).

6.2 Anisotropy-based inclination correction

The anisotropy-based inclination correction method of Jackson *et al.* (1991) (for magnetite) and Tan *et al.* (2003) (for haematite) is another widely used, and recently improved, method for assessing and correcting inclination biases in sedimentary rocks (Kodama 1997, 2009; Hodych *et al.* 1999; Tan 2001; Tan & Kodama 2002; Tan *et al.* 2003; Vaughn *et al.* 2005; Bilardello & Kodama 2009, 2010a,b,c; Bilardello *et al.* 2011). Comparative studies show that these two methods provide correction values that are consistent within error (Tauxe *et al.* 2008). The anisotropy-based inclination correction relies on the experimental measurement of remanence and particle anisotropies of the sedimentary rocks. The bulk anisotropies can be AMS, AARM or high-field anisotropy of IRM (hf-AIR). Direct measurement of the individual magnetic particle anisotropy is difficult because it requires specialized laboratory equipment. Kodama (2009) recently developed a simplified method for determining individual particle anisotropy for both haematite and magnetite; this method appears to be as accurate as the direct experimental measurement. We use this simplified method of Kodama (2009) to estimate the individual particle anisotropy of the magnetic carrier.

Our rock magnetic experiments described above demonstrate that the major magnetic carrier in Unit T_3 is Ti-poor magnetite. Therefore, we use the following applied theoretical expression to describe the particle anisotropy

$$\tan I_o/\tan I_c = [K_{min}(a + 2) - 1]/[K_{max}(a + 2) - 1], \quad (1)$$

where I_c is the corrected inclination, K_{max} and K_{min} are the maximum and minimum normalized eigenvalues, respectively and a is the individual particle anisotropy, which can be either a_γ (for remanence) or a_χ (for susceptibility; Jackson *et al.* 1991). In effect, a_γ and a_χ are estimated with a least-squares fit of the sample AARMs and AMS to the theoretical anisotropy expression. More details about this method can be found in Kodama (2009). In the least-squares fit, the rms error decreases monotonically with decreasing values of either a_γ or a_χ (Figs 11a and d). The critical values of $a_\gamma = 1.39$ and $a_\chi = 1.24$ are reached when theoretical values calculated from the right-hand side of eq. (1) using lower a_γ or a_χ values become negative for at least one sample in the data set. Individual particle anisotropies lower than 1.39 (for remanence) or 1.24 (for susceptibility) will make $[K_{min}(a + 2) - 1] < 0$ for samples having a lower K_{min}, which is incompatible with the range of measured anisotropies for these samples (Kodama 2009). Therefore, $a_\gamma = 1.39$ and $a_\chi = 1.24$ are the best fits to the curves. The $\tan I_o/\tan I_m$ fit the theoretical curves for $a_\gamma = 1.39$ much better than for $a_\gamma = 5$ and for $a_\chi = 1.24$
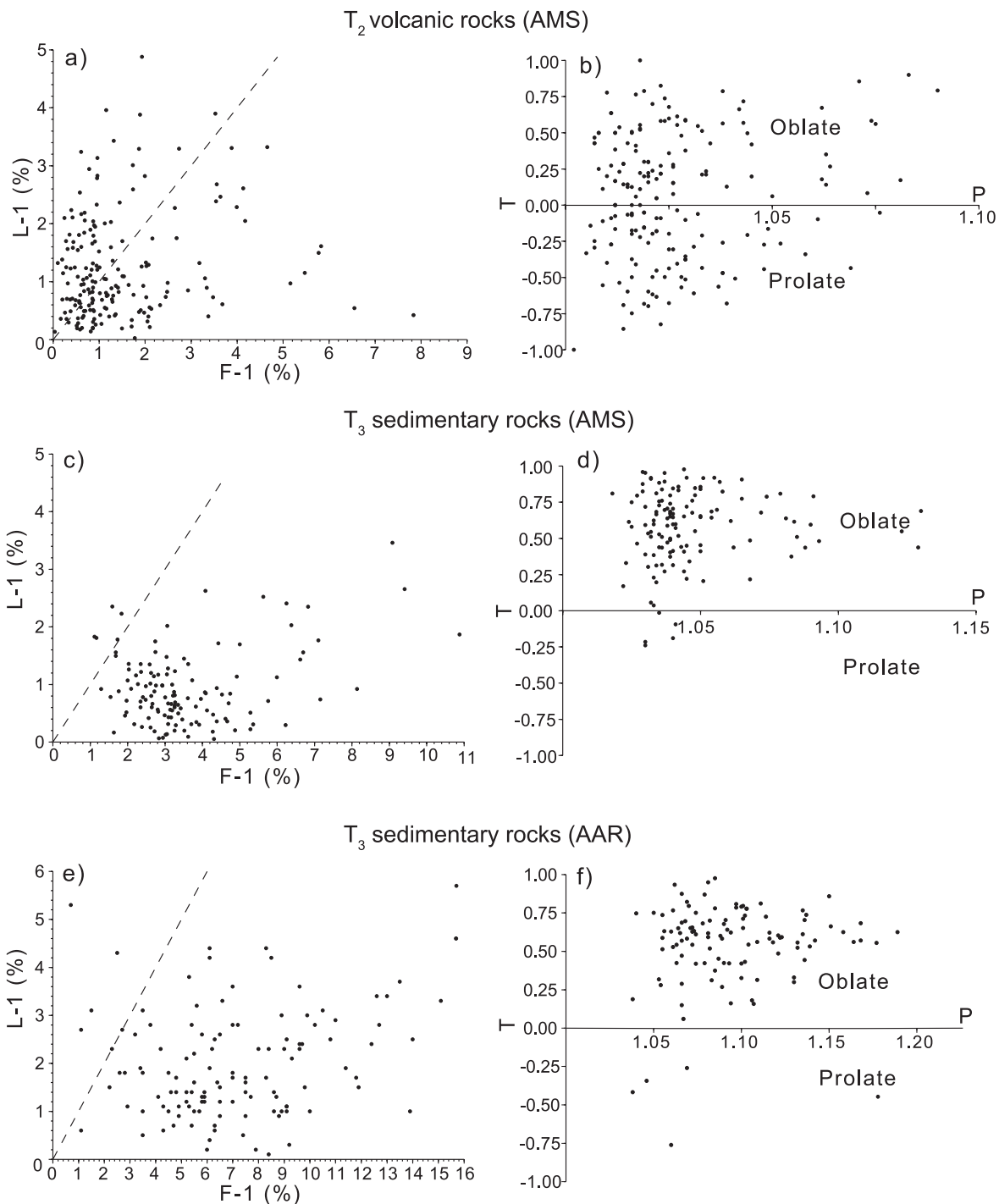
Figure 9. (a) Lineation versus Foliation (Flinn diagram) for the T_2 volcanic rocks from the AMS measurement. (b) *P* versus *T* plot for Unit T_3 sedimentary rocks from the AMS measurement. $P = K_{max}/K_{min}$, $T = (\ln F - \ln L)/(\ln F + \ln L)$, $F = K_{int}/K_{min}$, $L = K_{max}/K_{int}$ (Jelinek 1981). (c) Flinn diagram for Unit T_3 samples from the AMS measurement. (d) *P* versus *T* plot for Unit T_3 samples from the AMS measurement. (e) Flinn diagram for Unit T_3 sedimentary rocks from the AARM measurement. (f) *P* versus *T* plot for Unit T_3 samples from the AARM measurement.

much better than for $a_\chi = 3$ (Figs 11b and e). We also note that $a_\chi = 1.24$ is lower than $a_\gamma = 1.39$; this is reasonable because the effect of paramagnetic or diamagnetic minerals in the samples bias the measured AMS to be relatively lower than AARM and thus cause a slightly higher K_{min} as expected in the present case of an oblate triaxial ellipsoid.

Because the curve fitting may be biased by its reliance on the single minimum value of the data sets (de Groot *et al.* 2007),

we evaluate the reliability of this curve fitting determined particle anisotropies (a_γ and a_χ) using an alternative approach. We calculated the particle anisotropy for each specimen according to eq. (1), where I_c was obtained from the *E/I* method. From the AARM data, the calculated a_γ varies from 1.14 to 2.02 with a mean of 1.40, which is identical with the curve fitting result of 1.39 within the 95 per cent confidence interval. Using the same procedure, a lower a_χ was found ranging from 1.08 to 1.77 with a mean of 1.19. This
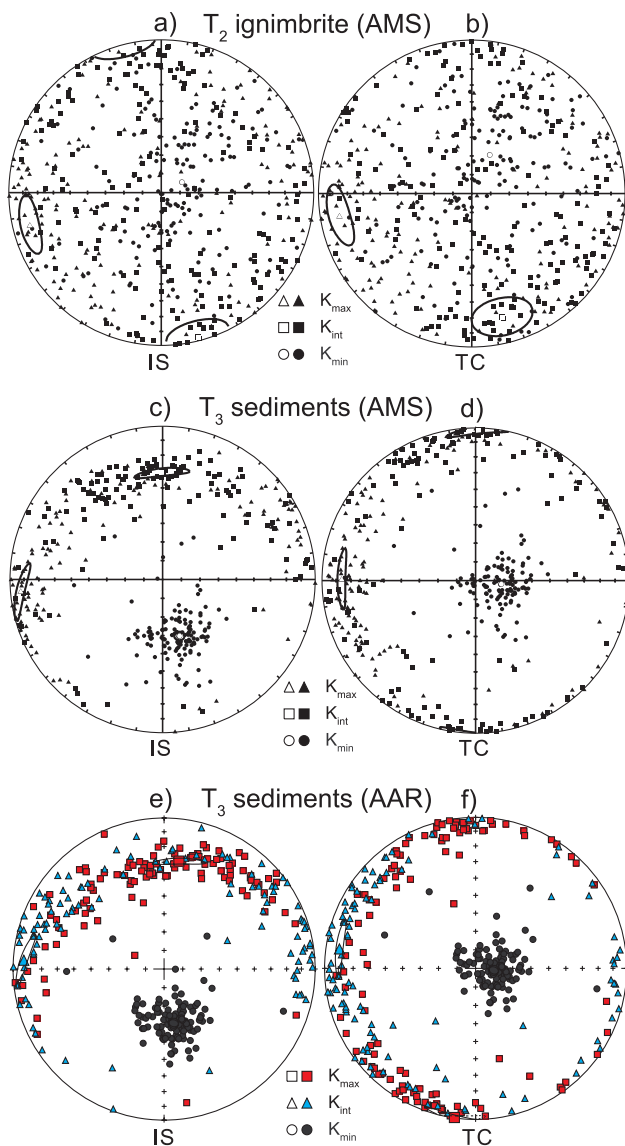
Figure 10. Stereoplots (equal area, lower-hemisphere projection) showing AMS data from the T_2 volcanic rocks, as well as AMS and AARM data from the T_3 sedimentary rocks. Maximum, intermediate, and minimum principal anisotropy axes are indicated, respectively, by triangles, squares and circles for AMS data and, respectively, by squares, triangles and circles for AARM data. Solid symbols show individual directions; open symbols are mean directions, with 95 per cent confidence zones indicated. tc, tilt correction; is, *in situ* (without tilt correction).

mean value is significantly different from the curve fitting result of 1.24. This further suggests the curve fitting-determined value of a_γ is a better representation than a_χ of the true particle anisotropy.

When $a_\gamma = 1.39$ is applied sample by sample to the ChRMs determined from Unit T_3 sedimentary rocks, we calculate a mean corrected direction of $D = 9.2°, I = 41.3°$ $(k = 20.2, \alpha_{95} = 3.3°)$. The A_{95} value of the mean corrected VGP of 96 directions is 3.2°, which falls well within the Deenen *et al.* (2011) confidence envelope for $N = 96$ of $A95_{\min/\max}$ of 2.7°/4.6° (Fig. 11c). For $a_\chi = 1.24$, we calculate a shallower mean corrected direction of $D = 9.2°, I = 34.5°$ $(k = 21.6, \alpha_{95} = 3.2°$; Fig. 11f). A simple F-test indicates that these corrected directions are significantly different from each other at the 95 per cent confidence level (p value: 0.15). The slight difference in declination arises from the fact that the available database from the

AMS and ARM is slightly different. For the ARM-based correction, the database consisted of 96 of the total selected 119 samples used for original mean ChRM calculation, whereas the number is 94 for AMS-based correction. We note that AARM inclination corrections are generally regarded as more accurate than those determined using AMS, because of biasing related to paramagnetic or diamagnetic anisotropy. Importantly, neither anisotropy-based corrected direction is significantly different from the direction corrected using the E/I method, and none of the corrected inclinations are significantly different at high confidence levels from the inclination measured in the underlying T_2 volcanics.

7 STRATIGRAPHIC INTERPRETATIONS OF MAGNETIC PROPERTIES

We now investigate the stratigraphic variation of magnetic properties and magnetic inclination within the measured section to identify potential inclination shallowing mechanisms (Fig.12).

7.1 Size and abundance of magnetic minerals

The susceptibility, NRM intensity and ARM intensity provides additional information about the size and abundance of the magnetic minerals. For samples from the top of Unit T_2 volcanic rocks and Unit T_3 sedimentary rocks, the initial intensities of the NRM range from 2 to 680 mA m^{-1}, ARM intensities (JARM) from 6.2 to 2100 mA m^{-1}, and magnetic susceptibilities (k) from 1 to 32 × 10^{-3} SI (Tables S4, S5 and S6). There are no remarkable differences between the top of Unit T_2 and Unit T_3. Initial NRM intensities generally increases with stratigraphic level, although samples from the top of Unit T_2 and the top of Unit T_3 show anomalously high values; magnetic susceptibility and ARM intensities show similar trends despite larger within-data set variability (Figs 12a–c).

The magnetization and susceptibility of magnetite are approximately 1000 times greater than most other ferromagnetic minerals (Collinson 1983), so we infer that the abundance of the main remanence carrier (Ti-poor titanomagnetite) increases upward in the section. This conclusion is supported by a plot of k versus XARM (JARM/0.05mT). In this diagram, the mean values of every 1/5 part of the whole section plot on the line defined by individual points. Meanwhile, the lowest interval (20.2–36.5 m) lies closest to the origin and the uppermost interval (182.1–225.9 m) lies farthest away (Fig. 13). Plotting of k versus XARM distinguishes magnetite grain size and abundance, with points falling on the same line passing through the origin indicative of uniform grain size and points falling farther from the origin indicative of greater magnetite abundance (King *et al.* 1982, 1983; Jackson *et al.* 1988). Therefore, it is likely that, on average, the magnetite grain size is relatively constant but the quantity of magnetic particles contributing to the remanence increases up-section.

7.2 Anisotropy parameters

In general, the distinct stratigraphic variations and preservation of sedimentary fabrics further suggest no tectonic overprint and that the ChRM is not the result of a secondary magnetization. In particular, we note the stratigraphic change in anisotropy parameters in Unit T_3 from 42 to 172 m, the interval of redbed deposition (Fig. 12). The top of the section (stratigraphic levels higher than 172 m) is principally constituted of green mud that may not be
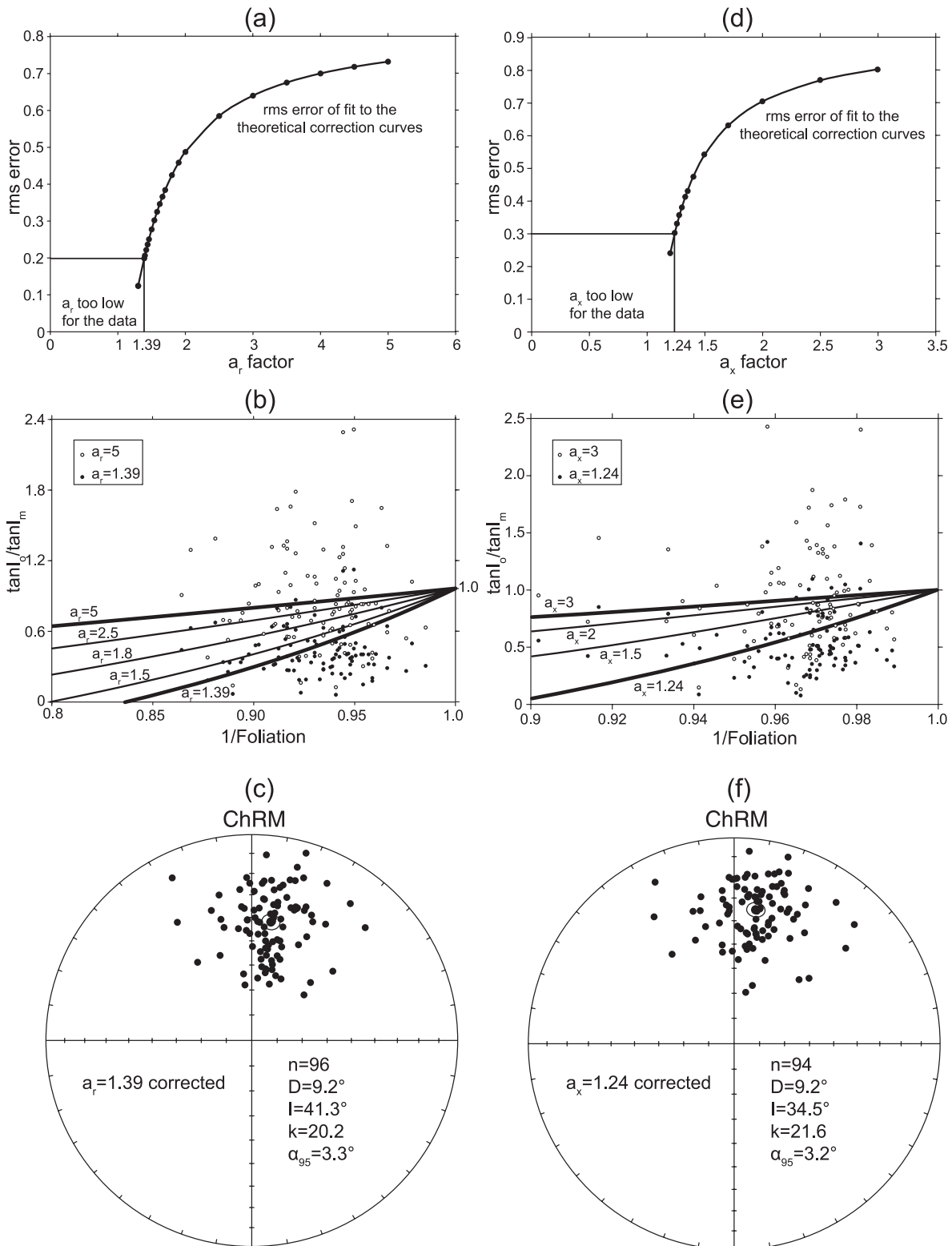
Figure 11. (a) Least-squares curve fitting of sample remanence anisotropy data to the theoretical inclination correction curves for magnetite (Jackson *et al.* 1991) for the 96 ChRM directions and their measured AARM anisotropies of the T_3 sedimentary rocks. The rms error decreases until $a_\gamma = 1.39$. Smaller values of a_γ are inconsistent with the AAR data (see text). The lowest rms error therefore occurs at $a_\gamma = 1.39$. (b) The fit of inclination data corrected with $a_\gamma = 5$ (circles) and 1.39 (dots) to the Jackson *et al.* (1991) theoretical correction curves, see eq. (1) in the text. (c) Equal-area projections of the individual ChRM directions after correction with $a_\gamma = 1.39$. (d) Least-squares curve fitting of sample susceptibility anisotropy data to the theoretical inclination correction curves for magnetite (Jackson *et al.* 1991) for the 94 ChRM directions and their measured susceptibility anisotropy of the T_3 samples. The rms error decreases until $a_\chi = 1.24$. Smaller values of a_γ are inconsistent with the AARM data (see text). The lowest rms error therefore occurs at $a_\chi = 1.24$. (e) The fit of inclination data corrected with $a_\chi = 3$ (circles) and 1.24 (dots) to the Jackson *et al.* (1991) theoretical correction curves, see eq. (1) in the text. (f) Equal-area projections of the individual ChRM directions after correction with $a_\chi = 1.24$.
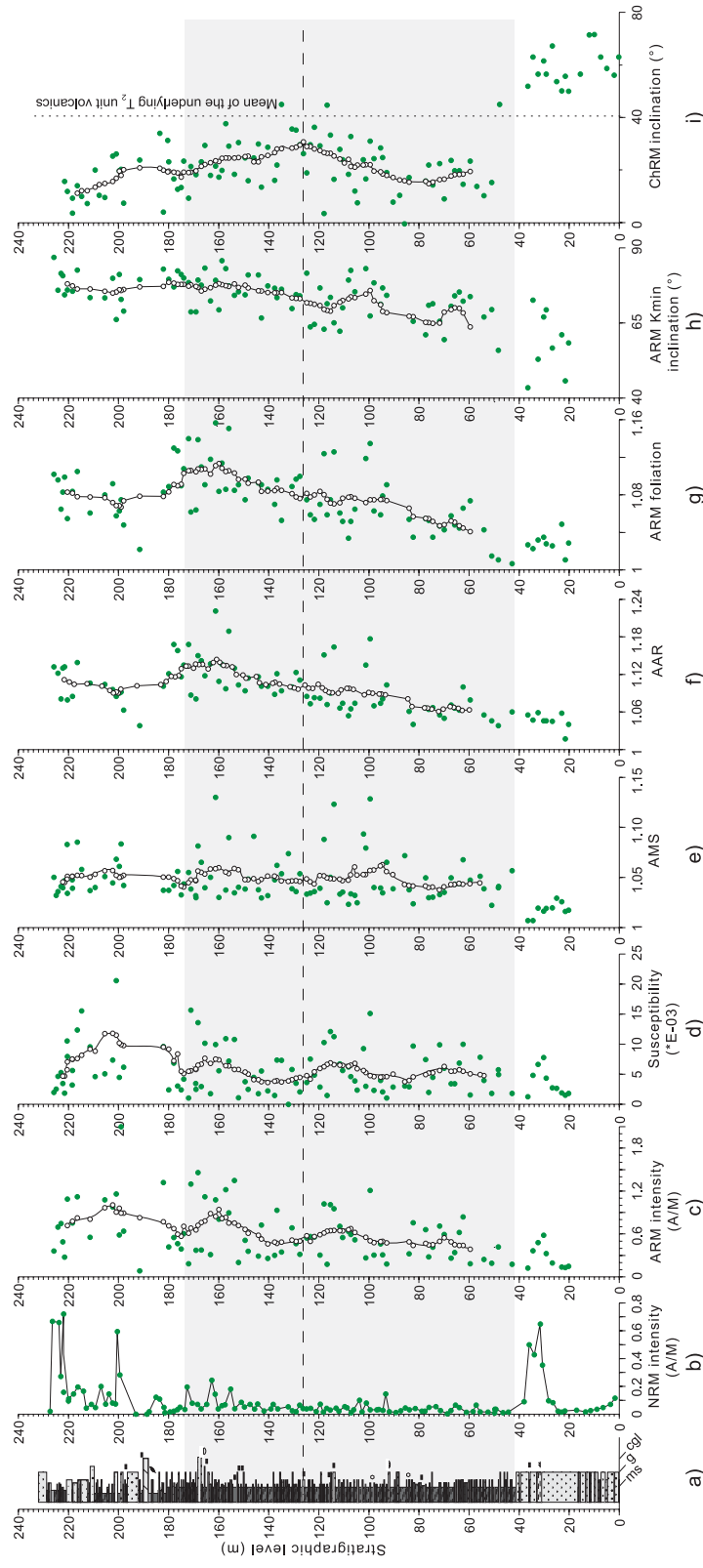
Figure 12. (a) Lithostratigraphy for the top of Unit T_2 and Unit T_3. Natural remanent magnetization (NRM) intensity, Anhysteretic remanent magnetization (ARM) intensity (c), bulk susceptibility (d), anisotropy of magnetic susceptibility (AMS) (e), anisotropy of anhysteretic remanent magnetization (AARM) (f), foliation of anhysteretic remanent magnetization (ARM) (g), inclination of minimum ARM axis (K_{min}) (h) and ChRM inclination (i) plotted against depth (0 is bottom; 240 m is top). Dots are the measured values; circles linked by short line are the mean values of every ten adjacent measured values. Note that the anomalously high ChRM inclinations of the tuff layers from the top of Unit T_2 probably reflects secular variation as interpreted by Dupont-Nivet *et al.* (2010b).
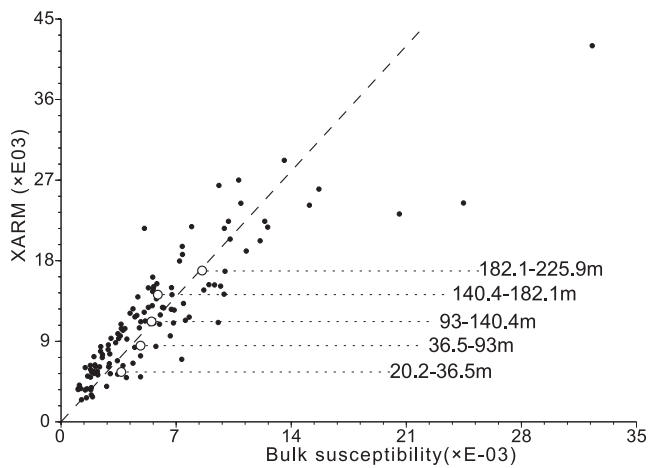
Figure 13. Normalized anhysteretic remanent magnetization intensity (ARM intensity/0.05 mT) plotted against bulk susceptibility (dots). Circles are mean values of each fifth of the 240-m-thick section (20.2–36.5 m is the bottom; 182.1–225.9 m is the top). Nomeste that mean values lie on the same slope as the individual dots.

comparable to the redbed interval due to a different depositional environment.

The degree of anisotropy and magnetic foliation appear to generally increase up-section throughout the redbed interval. The general up-section increase in P and F suggests that compaction (and/or depositional features due to the higher clay content/smaller grain size) increases up-section (Sun & Kodama 1992). This is consistent with the field observation that sediments at the bottom of this interval are coarser than those from the upper part that are more clay rich; coarser sediments generally experience less compaction than fine sediments. We also note that the inclination of the direction of K_{min} of the AARM and AMS both increase up-section. Assuming only compaction and imbrications processes affected the anisotropy orientation, the inclination of the K_{min} direction can indicate the respective effects of (1) sedimentary imbrication yielding a steeper mean K_{min} direction and (2) compaction rotating the mean K_{min} direction towards a vertical bedding-normal direction. Accordingly, the observed up-section increase in K_{min} inclination suggests an up-section increase in magnitude of compaction and decrease in the degree of imbrication. The implications of these results on the potential effect of sedimentary processes on inclination shallowing are discussed below.

8 DISCUSSION

8.1 Potential processes causing inclination shallowing

In contrast to the monotonic up-section increase of the anisotropy parameters, the ChRM inclinations generally increase between the 42 to the 126 m level and then decrease between the 126 to the 172 m level (Fig. 12). We suggest that the stratigraphic trends in inclination correspond to variations in inclination shallowing rather than secular variation of the geomagnetic field or apparent polar wander given the time frame of these changes and their intrinsic variations. Therefore, we interpret the trends in inclination shallowing in terms of variations in sedimentary compaction and imbrication.

In the upper part of the section (126–172 m level), low ChRM inclinations correspond to greater compaction and lower imbrication (inferred from the magnitude of L, F and K_{min} of both the AMS and AARM, see above). This relationship suggests a simple

and expected compaction-induced inclination shallowing for fine sediments, as documented by previous studies (King & Rees 1966; Owens 1974; Hrouda 1991; Jackson *et al.* 1991; Tan & Kodama 1998; Hrouda & Jezek 1999).

An opposite trend is observed in the lower part (42–126 m level), however, with ChRM inclinations generally increasing as indicators of compaction and imbrication, respectively, increase and decrease up-section. We interpret this to reflect the dominance of the imbrication over compaction on the inclination shallowing effect in this lower, coarser-grained interval. In the lower part of our record from the Linzhou basin, coarse-grained sands, flute casts, tool marks, and trough cross-stratification all suggest a hydrodynamic regime with greater energy than the finer-grained more laminated clays higher in the section. Therefore, imbrication probably dominates over compaction as a mechanism for shallowing primary inclinations in this more hydrodynamic part. Numerous redeposition experiments have documented inclination shallowing in excess of 30° due to sedimentary imbrication (King 1955; Griffiths *et al.* 1962; Hamilton & King 1964; Rees & Woodall 1975; Løvlie & Torsvik 1984). Gilder *et al.* (2001) argued that sedimentary imbrication is responsible for anomalously shallow inclinations measured in the Oligocene-Miocene redbeds from Subei, NW China. We note, however, that the east-directed palaeocurrents observed in our section are perpendicular to the northward ChRM direction. Thus, palaeocurrents may not be the sole factor affecting the ChRM inclinations.

Numerical depositional experiments indicate that faster sedimentation rates can also produce more inclination shallowing than slower rates (Jezek & Gilder 2002). This observation was used to explain the fact that Cretaceous redbeds in North and South China do not suffer inclination shallowing as much as those in central Asia (Gilder *et al.* 2003). Similarly, Jezek & Gilder (2006) suggested that the much shallower mean inclination measured in Neogene sedimentary rocks from the southern flank of the Tianshan compared to inclinations measured in coeval sedimentary unit from the northern flank was partly attributable to higher average sedimentation rates on the southern flank. Although we cannot assess accumulation rates in the studied section, sediments in the lower part are coarser than in the upper part, indicating a faster hydrodynamic condition and possibly a higher sedimentation rate that may have contributed to inclination shallowing in the lower part.

In summary, depositional processes appear to dominate the inclination shallowing in the lower interval. The observed inclination increases up-section as the degree of imbrication decreases until compaction, a depositional feature due to the higher clay content/smaller grain size, or both become the dominating factor and inclinations values decrease in the upper intervals. Ultimately, it appears that inclination shallowing processes in the T_3 sedimentary rocks are related to sediment grain size and depositional environments.

8.2 Using shallowing-corrected inclinations for India–Asia palaeogeography

Our results document inclination shallowing in the upper sedimentary successions of Linzizong Group in the Linzhou basin. Using the E/I correction by Tauxe & Kent (2004) and the anisotropy-based inclination correction by Kodama (2009), the measured inclination in the T_3 sedimentary rocks has been corrected from 20.5 ± 2.6° to 40.0° with 95 per cent confidence limits between 33.1° and 49.5° and to 41.3 ± 3.3°, respectively. These corrected inclinations are statistically indistinguishable from the 40.3 ± 4.5° mean inclination measured in the volcanic rocks immediately and conformably

below these sedimentary units (Dupont-Nivet *et al.* 2010b). Collectively, these palaeomagnetic results from the upper Linzizong Group indicate that the palaeolatitude of the southern Lhasa terrane from 55 to 43 Ma was ∼20°N (assuming a 100 per cent geocentric axial dipole field). Our results are consistent with recent reviews of robust palaeomagnetic data from Cretaceous and younger volcanic and other shallowing-corrected sedimentary rocks from the Lhasa terrane (van Hinsbergen *et al.* 2012; Lippert *et al.* in press).

Two published studies have applied inclination shallowing correction methods to sedimentary rocks from southern Tibet and provide a comparison of the magnitude of inclination shallowing in this region. Tan *et al.* (2010) used the *E/I* method to correct 377 directions from redbeds from the late Cretaceous Takena formation in the Linzhou basin and calculated a mean inclination of 42.0° with 95 per cent confidence limits between 39.9° and 44.5°; this value is much steeper than the initial mean inclination of 24.5°. van Hinsbergen *et al.* (2012) and Lippert *et al.* (in press) used the *E/I* technique to re-evaluate the 100 individual palaeomagnetic directions from redbeds from the late Cretaceous Shexing formation (Sun *et al.* 2012). They calculated a mean corrected inclination of 40.5° (33.3–47.7° 95 per cent confidence interval); the measured inclination is 31.2°. These corrected results are similar to our corrected inclination from Unit T_3 sedimentary rocks and the mean inclination of the T_2 volcanics, indicating that palaeolatitude of Lhasa terrane has remained remarkably stable from the late Cretaceous until early Eocene (see also Lippert *et al.* in press). In addition, the *E/I* method was also applied to upper Cretaceous to Palaeocene marine mudstones and limestones from Tethyan Himalayan, and showed that these sedimentary rocks have negligible (<5°) amounts of inclination shallowing and can therefore be used to estimate the palaeolatitude of Greater India before collision (Dupont-Nivet *et al.* 2010b; Yi *et al.* 2011; van Hinsbergen *et al.* 2012). Ultimately these studies have refined estimates on the timing and palaeolatitude of the collision to 51 ± 5 Ma at ∼20 ± 4°N (Lippert *et al.* in press). Our study and others that have addressed inclination shallowing show the general magnitude of shallowing we might expect in Cretaceous–Palaeogene rocks from this region and that the magnitude of shallowing depends on lithology.

Given the evidence for inclination shallowing in the sedimentary rocks from the Linzizong Group, the results reported by Chen *et al.* (2010) from sedimentary rocks from Nianbo formation (61–54 Ma) should also be reevaluated. More generally, because inclination shallowing in sedimentary rocks from southern Tibet is well-documented and demonstrably prevalent, we suggest that published palaeolatitudes determined from sedimentary units in this region that have not been evaluated for shallowing biases must be reconsidered before they are used in palaeogeographic reconstructions (Pozzi *et al.* 1982; Westphal & Pozzi 1983; Lin & Watts 1988; Chen *et al.* 1993, 2010; Patzelt *et al.* 1996). Future palaeomagnetic studies of sedimentary units from this region should take care to collect large sample sets and address potential depositional biasing effects. Finally, we note that the combination of data from volcanic and shallowing-corrected sedimentary rocks can provide more a robust palaeolatitude determination than a section of exclusively volcanic rocks that, although immune from depositional shallowing processes, may not sample enough time to average geomagnetic secular variation.

9 CONCLUSION

The large ∼20° discrepancy between the measured inclinations in approximately coeval volcanic rocks and sedimentary rocks strongly suggests inclination shallowing is present in Eocene sedimentary units from the Linzizong Group. This shallow biasing can be successfully corrected using two independent methods: (1) the *E/I* technique, based on the palaeosecular variation of geomagnetic field models (Tauxe & Kent 2004) and (2) the remanence anisotropy method, relying on the measurement of the magnetic anisotropy of a specimen and the individual magnetic particle anisotropy (Tan *et al.* 2003; Kodama 2009). Comparing the corrected inclinations from Unit T_3 sedimentary rocks to inclinations measured in Unit T_2 volcanics provides an independent check on the validity of the two types of corrections. The corrected inclinations from the two methods is in excellent agreement with the robust mean inclination of the underlying Unit T_2 volcanics (Dupont-Nivet *et al.* 2010b), which is in principle immune to inclination shallowing assuming that palaeosecular variation has been averaged. Our primary conclusions therefore are (i) a validation of the inclination shallowing correction methods; (ii) the consistency of shallowing corrections in upper Linzizong Group sedimentary unit and (iii) the presence of inclination shallowing in sedimentary rocks from southern Tibet requires systematic correction to generate meaningful palaeogeographies.

More generally, our results provide insight into sedimentary processes involved in the inclination shallowing and the application of correction methods. It may be argued that our results are fortuitous and that these methods may not apply to other sedimentary environments, rock types or magnetic mineralogies. Indeed, our thorough rock magnetic analyses show that the redbeds of Unit T_3 have a simple magnetic mineralogy dominated by titanomagnetite throughout the section. However, it is remarkable that these correction methods perform so well despite variation in depositional environments and sedimentary grain size observed through the fining upward section. Moreover, we provide evidence for a combination of processes including depositional and/or post depositional compaction and particle imbrication during deposition that may have affected inclination shallowing differently throughout the studied section. The successful corrections underline the robustness of the two independent methods.

An important result of our study is the depositional control on inclination shallowing. Overall, we observe a shallowing factor of ∼0.43 [*f* factor defined using King's (1955) equation], which means that these sedimentary rocks have undergone significantly more flattening than most of the reported magnetite-bearing sedimentary rocks with f factors ranging from 0.56 to 0.79 (Kodama & Davi 1995; Kodama 1997, 2009; Tan & Kodama 1998; Kim & Kodama 2004; Li *et al.* 2004; Vaughn *et al.* 2005; Bilardello & Kodama 2010a). It is becoming increasingly common to assume a flattening factor and apply a blanket (or even '*ad hoc*') correction using f factors of ∼0.6 (Kent & Irving 2010; Domeier *et al.* 2011). Inclination shallowing corrections must be supported by measuring remanence anisotropy, applying the *E/I* technique, or both.

We note that thorough rock magnetic analyses should be performed to determine the magnetic mineralogy throughout the studied sedimentary successions as we have done, in particular for using the magnetic particle anisotropy method. For that inclination correction method, our analyses indicate superior results when using AARM rather than AMS, which makes this method more suitable for magnetite type mineralogies. Inclination shallowing correction methods also have been shown to perform well with other magnetic mineralogies (in particular haematite), different depositional environments and rock types and at various latitudes (Bijaksana & Hodych 1997; Kodama 1997a; Tan & Kodama 1998, 2002; Hodych *et al.* 1999; Hodych & Bijaksana 2002; Tan *et al.* 2003; Krijgsman

& Tauxe 2004; Tauxe 2005; Vaughn *et al.* 2005; Yan *et al.* 2005; Bilardello & Kodama 2009, 2010a,b; Kodama 2009; Tan *et al.* 2010). We conclude that, when thoroughly constrained by rock magnetic analyses, shallowing-corrected palaeomagnetic results from sedimentary rocks can provide reliable palaeolatitude reconstructions and should therefore be systematically applied at least to test for the presence of shallowing.

REFERENCES

Achache, J., Courtillot, V. & Xiu, Z.Y., 1984. Paleogeographic and tectonic evolution of southern Tibet since middle Cretaceous time: new paleomagnetic data and synthesis, *J. geophys. Res.,* **89,** 10 311–10 310, 10 339.

Allegre, C.J., Courtillot, V., Tapponnier, P., Hirn, A. & Mattauer, M., 1984. Structure and evolution of the Himalaya-Tibet orogenic belt, *Nature,* **307,** 17–22.

Appel, E. & Soffel, H.C., 1984. Model for the domain state of Ti-rich titanomagnetites, *Geophys. Res. Lett.,* **11,** 189–192.

Bazhenov, M.L. & Mickolaichuck, A.V., 2002. Paleomagnetism of Paleogene basalts from the Tien Shan, Kyrgyzstan: rigid Eurasia and dipole geomagnetic field, *Earth planet. Sci. Lett.,* **195,** 155–166.

BGMRXAR (Bureau of Geology and Mineral Resources of Xizang Autonomous Region), 1993. *Regional Geology of Xizang (Tibet) Autonomous Region*, *Geological Memoirs Series,* Vol. 1, Number 31, Geological Publishing House, Beijing, 707 pp.

Bijaksana, S. & Hodych, J.P., 1997. Comparing remanence anisotropy and susceptibility anisotropy as predictors of paleomagnetic inclination shallowing in turbidites from the Scotian Rise, *Phys. Chem. Earth,* **22,** 189–193.

Bilardello, D. & Kodama, K.P., 2009. Measuring remanence anisotropy of hematite in red beds: anisotropy of high-field isothermal remanence magnetization (hf-AIR), *Geophys. J. Int.,* **178,** 1260–1272.

Bilardello, D. & Kodama, K.P., 2010a. Rock magnetic evidence for inclination shallowing in the early Carboniferous Deer Lake Group red beds of western Newfoundland, *Geophys. J. Int.,* **181,** 275–289.

Bilardello, D. & Kodama, K.P., 2010b. A new inclination shallowing correction of the Mauch Chunk Formation of Pennsylvania, based on high-field AIR results: implications for the Carboniferous North American APW path and Pangea reconstructions, *Earth planet. Sci. Lett.,* **299,** 218–227.

Bilardello, D. & Kodama, K.P., 2010c. Palaeomagnetism and magnetic anisotropy of Carboniferous red beds from the Maritime Provinces of Canada: evidence for shallow palaeomagnetic inclinations and implications for North American apparent polar wander, *Geophys. J. Int.,* **180,** 1013–1029.

Bilardello, D., Jezek, J. & Kodama, K.P., 2011. Propagating and incorporating the error in anisotropy-based inclination corrections, *Geophys. J. Int.,* **187,** 75–84.

Burg, J.P. & Chen, G.M., 1984. Tectonics and structural zonation of southern Tibet, China. *Nature,* **311,** 219–223.

Burg, J.P., Proust, F., Tapponnier, P. & Chen, G.M., 1983. Deformation phases and tectonic evolution of the Lhasa block (southern Tibet, China), *Eclogae Geol. Helvetiae,* **76,** 643–665.

Chauvin, A., Perroud, H. & Bazhenov, M.L., 1996. Anomalous low palaeomagnetic inclinations from Oligocene-Lower Miocene red beds of the south-west Tien Shan, Central Asia, *Geophys. J. Int.,* **126,** 303–313.

Chen, J., Huang, B. & Sun, L., 2010. New constraints to the onset of the India-Asia collision: paleomagnetic reconnaissance on the Linzizong Group in the Lhasa Block, China, *Tectonophysics,* **489,** 189–209.

Chen, W. *et al.*, 2012. Paleomagnetic results from the Early Cretaceous Zenong Group volcanic rocks, Cuoqin, Tibet, and their paleogeographic implications, *Gondwana Res.,* **22,** 461–469.

Chen, Y., Cogne, J.P., Courtillot, V., Tapponnier, P. & Zhu, X.Y., 1993. Cretaceous paleomagnetic results from western Tibet and tectonic implications, *J. geophys. Res.,* **98,** 17–17.

Collinson, D.W., 1983. *Methods in rock Magnetism and Palaeomagnetism: Techniques and Instrumentation,* Vol. 503, Chapman and Hall, London.

Coulon, C., Maluski, H., Bollinger, C. & Wang, S., 1986. Mesozoic and Cenozoic volcanic rocks from central and southern Tibet: 39Ar-40Ar dating, petrological characteristics and geodynamical significance, *Earth planet. Sci. Lett.,* **79,** 281–302.

de Groot, L., Haldan, M. & Langereis, C., 2007. Inclination error correction in red beds: is it possible? *Eos Trans. AGU,* **88**(52), Fall Meet. Suppl., Abstract GP34A-03.

Deenen, M.H.L., Langereis, C.G., van Hinsbergen, D.J.J. & Biggin, A.J., 2011. Geomagnetic secular variation and the statistics of palaeomagnetic directions, *Geophys. J. Int.,* **186,** 509–520.

Dewey, J.F., Shackleton, R.M., Chengfa, C. & Yiyin, S., 1988. The tectonic evolution of the Tibetan Plateau, *Proc. R. Soc. Lond.,* **327,** 379–413.

Ding, L., Kapp, P., Zhong, D. & Deng, W., 2003. Cenozoic volcanism in Tibet: evidence for a transition from oceanic to continental subduction, *J. Petrol.,* **44,** 1833–1865.

Domeier, M., Van der Voo, R. & Denny, F.B., 2011. Widespread inclination shallowing in Permian and Triassic paleomagnetic data from Laurentia: support from new paleomagnetic data from Middle Permian shallow intrusions in southern Illinois (USA) and virtual geomagnetic pole distributions, *Tectonophysics,* **511,** 38–52.

Dunlop, D.J., 2002. Theory and application of the Day plot (Mrs/Ms versus Hcr/Hc) 1. Theoretical curves and tests using titanomagnetite data, *J. geophys. Res.,* **107,** 2056, doi:10.1029/2001JB000486.

Dunlop, D.J. & Ödemir, Ö., 1997. *Rock Magnetism: Fundamentals and Frontiers,* Cambridge University Press, Cambridge, 573 pp.

Dupont-Nivet, G., Guo, Z., Butler, R.F. & Jia, C., 2002. Discordant paleomagnetic direction in Miocene rocks from the central Tarim Basin: evidence for local deformation and inclination shallowing, *Earth planet. Sci. Lett.,* **199,** 473–482.

Dupont-Nivet, G., Hoorn, C. & Konert, M., 2008. Tibetan uplift prior to the Eocene-Oligocene climate transition: evidence from pollen analysis of the Xining Basin, *Geology,* **36,** 987–990.

Dupont-Nivet, G., van Hinsbergen, D.J.J. & Torsvik, T.H., 2010a. Persistently low Asian paleolatitudes: implications for the India-Asia collision history, *Tectonics,* **29,** TC5016, doi:10.1029/2008TC002437.

Dupont-Nivet, G., Lippert, P.C., van Hinsbergen, D.J.J., Meijers, M.J.M. & Kapp, P., 2010b. Palaeolatitude and age of the Indo-Asia collision: palaeomagnetic constraints, *Geophys. J. Int.,* **182,** 1189–1198.

Fisher, R.A., 1953. Dispersion on a sphere, *Proc. R. Soc. Lond., Ser. A: Math. Phys. Sci.,* **217,** 295–305.

Gilder, S., Chen, Y. & Sen, S., 2001. Oligo-Miocene magnetostratigraphy and rock magnetism of the Xishuigou section, Subei (Gansu Province, western China) and implications for shallow inclinations in central Asia, *J. geophys. Res.,* **106,** 30 505–30 522.

Gilder, S., Chen, Y., Cogne, J.-P., Tan, X., Courtillot, V., Sun, D. & Li, Y., 2003. Paleomagnetism of Upper Jurassic to Lower Cretaceous volcanic and sedimentary rocks from the western Tarim Basin and implications for inclination shallowing and absolute dating of the M-0 (ISEA?) chron, *Earth planet. Sci. Lett.,* **206,** 587–600.

Gradstein, F.M., Ogg, J.G., Schmitz, M. & Ogg, G., 2012. *The Geologic Time Scale 2012,* Elsevier, Amsterdam, 899 pp.

Griffiths, D.H., King, R.F. & Rees, A.I., 1962. The relevance of magnetic measurements on some fine grained silts to the study of their depositional process, *Sedimentology,* **1,** 134–144.

Hamilton, N. & King, R.F., 1964. Comparison of the bedding errors of artificially and naturally deposited sediments with those predicted from a simple model, *Geophys. J. R. astr. Soc.,* **8,** 370–374.

He, S., Kapp, P., DeCelles, P.G., Gehrels, G.E. & Heizler, M., 2007. Cretaceous-Tertiary geology of the Gangdese Arc in the Linzhou area, southern Tibet, *Tectonophysics,* **433,** 15–37.

Hodych, J.P. & Bijaksana, S., 2002. Plastically deforming clay-rich sediment to help measure the average remanence anisotropy of its individual magnetic particles, and correct for paleomagnetic inclination shallowing, *Phys. Chem. Earth, Parts A/B/C,* **27,** 1273–1279.

Hodych, J.P., Bijaksana, S. & Pätzold, R., 1999. Using magnetic anisotropy to correct for paleomagnetic inclination shallowing in some magnetite-bearing deep-sea turbidites and limestones, *Tectonophysics,* **307,** 191–205.

Housen, B.A., Richter, C. & Van Der Pluijm, B.A., 1993. Composite magnetic anisotropy fabrics: experiments, numerical models and implications for the quantification of rock fabrics, *Tectonophysics,* **220,** 1–12.

Hrouda, F. & Jezek, J., 1999. Magnetic anisotropy indications of deformations associated with diagenesis, *Geol. Soc., Lond., Spec. Publ.,* **151,** 127–137.

Hrouda, F.S., 1991. Models of magnetic anisotropy variations in sedimentary thrust sheets, *Tectonophysics,* **185,** 203–210.

Jackson, M., Gruber, W., Marvin, J. & Banerjee, S.K., 1988. Partial anhysteretic remanence and its anisotropy: applications and grainsize - dependence, *Geophys. Res. Lett.,* **15,** 440–443.

Jackson, M.J., Banerjee, J.A., Marvin, R.L. & Grueber, W., 1991. Detrital remanence inclination errors, and anhysteretic remanence anisotropy: quantitative model and experimental results, *Geophys. J. Int.,* **104,** 95–103.

Jelinek, V., 1981. Characterization of the magnetic fabric of rocks, *Tectonophysics,* **79,** T63–T67.

Jezek, J. & Gilder, S., 2002. Competition of magnetic and hydrodynamic forces on ellipsoidal particles under shear: potential influence on the recording process of the Earth's magnetic field in sediments, in *EGS General Assembly Conference,* Nice, France. Abstract 1421.

Jezek, J. & Gilder, S.A., 2006. Competition of magnetic and hydrodynamic forces on ellipsoidal particles under shear: influence of the Earth's magnetic field on particle alignment in viscous media, *J. geophys. Res.,* **111,** B12S23, doi:10.1029/2006JB004541.

Kapp, P., DeCelles, P.G., Gehrels, G.E., Heizler, M. & Ding, L., 2007. Geological records of the Lhasa-Qiangtang and Indo-Asian collisions in the Nima area of central Tibet, *Geol. Soc. Am. Bull.,* **119,** 917–933.

Kent, D.V. & Irving, E., 2010. Influence of inclination error in sedimentary rocks on the Triassic and Jurassic apparent pole wander path for North America and implications for Cordilleran tectonics, *J. geophys. Res.: Solid Earth (1978–2012),* **115,** B10103, doi:10.1029/2009JB007205.

Kent, D.V. & Smethurst, M.A., 1998. Shallow bias of paleomagnetic inclinations in the Paleozoic and Precambrian, *Earth planet. Sci. Lett.,* **160,** 391–402.

Kim, B. & Kodama, K.P., 2004. A compaction correction for the paleomagnetism of the Nanaimo Group sedimentary rocks: implications for the Baja British Columbia hypothesis, *J. geophys. Res.: Solid Earth (1978–2012).,* **109,** B02102, doi:10.1029/2003JB002696.

King, J.W., Banerjee, S.K., Marvin, J. & Ozdemir, O., 1982. A comparison of different magnetic methods for determining the relative grain size of magnetite in natural materials: some results from lake sediments, *Earth planet. Sci. Lett.,* **59,** 404–419.

King, J.W., Banerjee, S.K. & Marvin, J., 1983. A new rock-magnetic approach to selecting sediments for geomagnetic paleointensity studies: application to paleointensity for the last 4000 years, *J. geophys. Res.,* **88,** 5911–5921.

King, R.F., 1955. The remanent magnetism of artificially deposited sediments, *Geophys. J. Int.,* **7,** 115–134.

King, R.F. & Rees, A.I., 1966. Detrital magnetism in sediments: an examination of some theoretical models, *J. geophys. Res.,* **71,** 561–571.

Kirschvink, J.L., 1980. The least-square line and plane and the analysis of paleomagnetic data, *Geophys. J. R. astr. Soc.,* **62,** 699–718.

Kodama, K. & Davi, J., 1995. A compaction correction for the paleomagnetism of the Cretaceous Pigeon Point Formation of California, *Tectonics,* **14,** 1153–1164.

Kodama, K.P., 1997. A successful rock magnetic technique for correctng paleomagnetic inclination shallowing: case study of the nacimiento formation, New Mexico, *J. geophys. Res.,* **102,** 5193–5205.

Kodama, K.P., 2009. Simplification of the anisotropy-based inclination correction technique for magnetite- and haematite-bearing rocks: a case study for the Carboniferous Glenshaw and Mauch Chunk Formations, North America, *Geophys. J. Int.,* **176,** 467–477.

Krijgsman, W. & Tauxe, L., 2004. Shallow bias in Mediterranean paleomagnetic directions caused by inclination error, *Earth planet. Sci. Lett.,* **222,** 685–695.

Kruiver, P.P. & Passier, H.F., 2001. Coercivity analysis of magnetic phases in sapropel S1 related to variations in redox conditions, including an investigation of the S-ratio, *Geochem. Geophys. Geosyst,* **2,** 1063, doi:10.1029/2001GC000181.

Kruiver, P.P., Dekkers, M.J. & Heslop, D., 2001. Quantification of magnetic coercivity components by the analysis of acquisition curves of isothermal remanent magnetisation, *Earth planet. Sci. Lett.,* **189,** 269–276.

Løvlie, R. & Torsvik, T., 1984. Magnetic remanence and fabric properties of laboratory-deposited hematite-bearing red sandstone, *Geophys. Res. Lett.,* **11,** 221–224.

Lee, H.Y., Chung, S.-L., Wang, Y., Zhu, D., Yang, J., Song, B., Liu, D. & Wu, F., 2007. Age, petrogenesis and geological significance of the Linzizong volcanic successions in the Linzhou basin, southern Tibet: evidence from zircon U-Pb dates and Hf isotopes, *Acta Petrol. Sin.,* **23,** 493–500.

Lee, H.Y., Chung, S.L., Lo, C.H., Ji, J., Lee, T.Y., Qian, Q. & Zhang, Q., 2009. Eocene Neotethyan slab breakoff in southern Tibet inferred from the Linzizong volcanic record, *Tectonophysics,* **477,** 20–35.

Leier, A.L., DeCelles, P.G., Kapp, P. & Ding, L., 2007. The Takena formation of the Lhasa terrane, southern Tibet: the record of a Late Cretaceous retroarc foreland basin, *Geol. Soc. Am. Bull.,* **119,** 31–48.

Li, Y.X., Kodama, K.P. & Smith, D.P., 2004. New paleomagnetic, rock magnetic, and petrographic results from the Valle Group, Baja California, Mexico: exploring the causes of anomalously shallow paleomagnetic inclinations, *J. geophys. Res,* **109,** B11101, doi:10.1029/2004JB003127.

Liebke, U., Appel, E., Ding, L., Neumann, U., Antolin, B. & Xu, Q., 2010. Position of the Lhasa terrane prior to India-Asia collision derived from palaeomagnetic inclinations of 53 Ma old dykes of the Linzhou Basin: constraints on the age of collision and post-collisional shortening within the Tibetan Plateau, *Geophys. J. Int.,* **182,** 1199–1215.

Lin, J. & Watts, D.R., 1988. Paleomagnetic constrains on Himalayan-Tibetan tectonic evolution, *Phil. Trans. R. Soc. Lond.,* **326,** 177–188.

Lippert, P.C., Zhao, X.X., Coe, R.S. & Lo, C.H., 2011. Palaeomagnetism and Ar-40/Ar-39 geochronology of upper Palaeogene volcanic rocks from Central Tibet: implications for the Central Asia inclination anomaly, the palaeolatitude of Tibet and post-50 Ma shortening within Asia, *Geophys. J. Int.,* **184,** 131–161.

Lippert, P.C., van Hinsbergen, D.J.J. & Dupont-Nivet, G., in press. The Early Cretaceous to Present latitude of the central Lhasa-plano (Tibet): a paleomagnetic synthesis with implications for Cenozoic tectonics, paleogeography and climate of Asia, in *Towards an Improved Understanding of Uplift Mechanisms and the Elevation History of the Tibetan Plateau,* eds Nie, J.S., Hoke, G.D. & Horton, B.K., Geological Society of America Special Paper.

McCabe, C., Jackson, M. & Ellwood, B.B., 1985. Magnetic anisotropy in the Trenton limestone: results of a new technique, anisotropy of anhysteretic susceptibility, *Geophys. Res. Lett.,* **12,** 333–336.

Mo, X., Zhao, Z., Deng, J., Dong, G.C., Zhou, S., Guo, T.Y., Zhang, S.Q. & Wang, L.L., 2003. Response of volcanism to the India-Asia collision, *Earth Sci. Front.,* **10,** 135–148.

Mo, X., Hou, Z., Niu, Y., Dong, G., Qu, X., Zhao, Z. & Yang, Z., 2007. Mantle contributions to crustal thickening during continental collision: evidence from Cenozoic igneous rocks in southern Tibet, *Lithos,* **96,** 225–242.

Mo, X., Niu, Y., Dong, G., Zhao, Z., Hou, Z., Zhou, S. & Ke, S., 2008. Contribution of syncollisional felsic magmatism to continental crust growth: a case study of the Paleogene Linzizong volcanic succession in southern Tibet, *Chem. Geol.,* **250,** 49–67.

Mullender, T.A.T., Velzen, A.J. & Dekkers, M.J., 1993. Continuous drift correction and separate identification of ferrimagnetic and paramagnetic contributions in thermomagnetic runs, *Geophys. J. Int.,* **114,** 663–672.

Mullender, T.A.T., Frederichs, T., Hilgenfeldt, C., Fabian, K. & Dekkers, M.J., 2005. Fully automated demagnetization and measurement of NRM, ARM and IRM on a '2G' SQUID magnetometer, *IAGA Conference,* Toulouse, France. Abstract number: IAGA2005-A-00898.

Owens, W., 1974. Mathematical model studies on factors affecting the magnetic anisotropy of deformed rocks, *Tectonophysics,* **24,** 115–131.

Pares, J.M., van der Pluijm, B.A. & Dinares-Turell, J., 1999. Evolution of magnetic fabrics during incipient deformation of mudrocks (Pyrenees, northern Spain), *Tectonophysics,* **307,** 1–14.

Patzelt, A., Li, H., Wang, J. & Appel, E., 1996. Palaeomagnetism of Cretaceous to Tertiary sediments from southern Tibet: evidence for the extent of the northern margin of India prior to the collision with Eurasia, *Tectonophysics,* **259,** 259–284.

Pike, C.R., Roberts, A.P. & Verosub, K.L., 1999. Characterizing interactions in fine magnetic particle systems using first order reversal curves, *J. appl. Phys.,* **85,** 6660–6667.

Pozzi, J.-P., Westphal, M., Xiu Zhou, Y., Sheng Xing, L. & Yao Chen, X., 1982. Position of the Lhasa block, South Tibet, during the late Cretaceous, *Nature,* **297,** 319–321.

Rees, A.I., 1961. The effect of water currents on the magnetic remanence and anisotropy of susceptibility of some sediments, *Geophys. J. R. astr. Soc.,* **5,** 235–251.

Rees, A.I., 1965. The Use of Anisotropy of Magnetic Susceptibility in the Estimation of Sedimentary FABRIC1, *Sedimentology,* **4,** 257–271.

Rees, A.I. & Woodall, W.A., 1975. The magnetic fabric of some laboratory-deposited sediments, *Earth planet. Sci. Lett.,* **25,** 121–130.

Roberts, A.P., Pike, C.R. & Verosub, K.L., 2000. First-order reversal curve diagrams: a new tool for characterizing the magnetic properties of natural samples, *J. geophys. Res.,* **105,** 461–428.

Sengor, A.M.C., 1984. The Cimmeride orogenic system and the tectonics of Eurasia, *Geol. Soc. Am. Spec. Paper,* **195,** 1–74.

Si, J. & Van der Voo, R., 2001. Too-low magnetic inclinations in central Asia: an indication of a long-term Tertiary non-dipole field? *Terra Nova,* **13,** 471–478.

Sun, W.W. & Kodama, K.P., 1992. Magnetic anisotropy, scanning electron microscopy, and X-ray pole figure goniometry study of inclination shallowing in a compacting clay-rich sediment, *J. geophys. Res.,* **97,** 19 599–19 615.

Sun, Z., Jiang, W., Li, H., Pei, J. & Zhu, Z., 2010. New paleomagnetic results of Paleocene volcanic rocks from the Lhasa block: tectonic implications for the collision of India and Asia, *Tectonophysics,* **490,** 257–266.

Sun, Z., Pei, J., Li, H., Xu, W., Jiang, W., Zhu, Z., Wang, X. & Yang, Z., 2012. Palaeomagnetism of late Cretaceous sediments from southern Tibet: evidence for the consistent palaeolatitudes of the southern margin of Eurasia prior to the collision with India, *Gondwana Res.,* **21,** 53–63.

Tan, X., 2001. Correcting the bias toward shallow paleomagnetic inclinations in hematite-bearing sedimentary rocks: theory, experiments, and applications, *PhD thesis,* Lehigh University.

Tan, X. & Kodama, K.P., 1998. Compaction-corrected inclinations from southern California Cretaceous marine sedimentary rocks indicate no paleolatitudinal offset for the Peninsular Ranges terrane, *J. geophys. Res.,* **103,** 27 169–27 192.

Tan, X. & Kodama, K.P., 2002. Magnetic anisotropy and paleomagnetic inclination shallowing in red beds: evidence from the Mississippian Mauch Chunk Formation, Pennsylvania, *J. geophys. Res.,* **107,** 2311, doi:10.1029/2001JB001636.

Tan, X., Kodama, K.P., Chen, H., Fang, D., Sun, D. & Li, Y., 2003. Paleomagnetism and magnetic anisotropy of Cretaceous red beds from the Tarim basin, northwest China: evidence for a rock magnetic cause of anomalously shallow paleomagnetic inclinations from Central Asia, *J. geophys. Res.,* **108,** 2107, doi:10.1029/2001JB001608.

Tan, X., Gilder, S., Kodama, K.P., Jiang, W., Han, Y., Zhang, H., Xu, H. & Zhou, D., 2010. New paleomagnetic results from the Lhasa block: revised estimation of latitudinal shortening across Tibet and implications for dating the India-Asia collision, *Earth planet. Sci. Lett.,* **293,** 396–404.

Tapponnier, P., Mattauer, M., Proust, F. & Cassaigneau, C., 1981. Mesozoic ophiolites, sutures, and large-scale tectonic meovements in Afghanistan, *Earth planet. Sci. Lett.,* **52,** 355–371.

Tarling, D. & Hrouda, F., 1993. *Magnetic Anisotropy of Rocks,* Chapman & Hall, London.

Tauxe, L. & Kent, D.V., 2004. A simplified statistical model for the geomagnetic field and the detection of shallow bias in paleomagnetic inclinations: was the ancient magnetic field dipolar, *Timescales Paleomag. Field,* **145,** 101–115.

Tauxe, L., 2005. Inclination flattening and the geocentric axial dipole hypothesis, *Earth planet. Sci. Lett.,* **233,** 247–261.

Tauxe, L., Kodama, K.P. & Kent, D.V., 2008. Testing corrections for paleomagnetic inclination error in sedimentary rocks: a comparative approach, *Phys. Earth planet. Inter.,* **169,** 152–165.

Torsvik, T.H. & Van der Voo, R., 2002. Refining Gondwana and Pangea palaeogeography: estimates of phanerozoic (octupole) non-dipole fields, *Geophys. J. Int.,* **151,** 771–794.

Vandamme, D., 1994. A new method to determine paleosecular variation, *Phys. Earth planet. Inter.,* **85,** 131–142.

Van der Voo, R. & Torsvik, T.H., 2001. Evidence for late Paleozoic and Mesozoic non-dipole fields provides an explanation for the Pangea reconstruction problems, *Earth planet. Sci. Lett.,* **187,** 71–81.

van Hinsbergen, D.J.J., Lippert, P.C., Dupont-Nivet, G., McQuarrie, N., Doubrovine, P.V., Spakman, W. & Torsvik, T.H., 2012. Greater India Basin hypothesis and a two-stage Cenozoic collision between India and Asia, *Proc. Natl. Acad. Sci.,* **109,** 7659–7664.

Vaughn, J., Kodama, K.P. & Smith, D.P., 2005. Correction of inclination shallowing and its tectonic implications: the Cretaceous Perforada Formation, Baja California, *Earth planet. Sci. Lett.,* **232,** 71–82.

Westphal, M., 1993. Did a large departure from the geocentric axial dipole hypothesis occur during the Eocene? Evidence from the magnetic polar wander path of Eurasia, *Earth planet. Sci. Lett.,* **117,** 15–28.

Westphal, M. & Pozzi, J.-P., 1983. Paleomagnetic and plate tectonic constraints on the movement of Tibet, *Tectonophysics,* **98,** 1–10.

Xu, R.H., Scharer, U. & Allegre, C.J., 1985. Magmatism and metamorphism in the Lhasa block (Tibet): a geochronological study, *J. Geol.,* 41–57.

Yan, M., Voo, R.V.D., Tauxe, L., Fang, X. & Parés, J.M., 2005. Shallow bias in Neogene palaeomagnetic directions from the Guide Basin, NE Tibet, caused by inclination error, *Geophys. J. Int.,* **163,** 944–948.

Yi, Z., Huang, B., Chen, J., Chen, L. & Wang, H., 2011. Paleomagnetism of early Paleogene marine sediments in southern Tibet, China: implications to onset of the India-Asia collision and size of Greater India, *Earth planet. Sci. Lett.,* **309,** 153–165.

Yin, A. & Harrison, M.T., 2000. Geologic evolution of the Himalayan-Tibetan orogen, *Ann. Rev. Earth planet. Sci.,* **28,** 211–280.

Yuquans, Z., 1995. Thermal evolution of the Gangdese batholith, southern Tibet: a history of episodic unroofing, *Tectonics,* **14,** 223–236.

Zhou, S., Mo, X., Dong, G., Zhao, Z., Qiu, R., Guo, T. & Wang, L., 2004. 40 Ar-39 Ar geochronology of Cenozoic Linzizong volcanic rocks from Linzhou Basin, Tibet, China, and their geological implications, *Chin. Sci. Bull.,* **49,** 1970–1979.

SUPPORTING INFORMATION

Additional Supporting Information may be found in the online version of this article:

Table S1. Bedding orientations of the T_3 unit (see Fig. 2).

Table S2. Hysteresis parameters inferred from MicroMag measurements.

Table S3. Results of isothermal remanent magnetization (IRM) component analysis for the studied samples.

Table S4. Individual sample characteristic remanent magnetization (ChRM) directions by both thermal and alternating field demagnetization and mean directions (see Fig. 8).

Table S5. Results of the anisotropy of magnetic susceptibility (AMS) measurement of the sediments from the T_3 unit and lava flow from the T_2 unit.

Table S6. Results of the anisotropy of anhysteretic remanence (AAR) measurement of the sediments from the T_3 unit (http://gji.oxfordjournals.org/lookup/suppl/doi:10.1093/gji/ggt188/-/DC1).

Please note: Oxford University Press are not responsible for the content or functionality of any supporting materials supplied by the authors. Any queries (other than missing material) should be directed to the corresponding author for the article.